International Journal of Impact Engineering 177 (2023) 104490

Contents lists available at ScienceDirect

International Journal of Impact Engineering

journal homepage: www.elsevier.com/locate/ijimpeng

Neural network modelling of mechanical joints for the application in large-scale crash analyses

Victor André *, Miguel Costas, Magnus Langseth, David Morin

Structural Impact Laboratory (SIMLab) and Centre for Advanced Structural Analysis (CASA), Department of Structural Engineering, Norwegian University of Science and Technology (NTNU), NO-7491 Trondheim, Norway

ARTICLE INFO

Keywords:
Machine learning
Neural networks
Crash analysis
Finite element
Self-piercing rivet
Flow-drill screw

ABSTRACT

This paper presents an artificial neural network (NN) modelling approach to represent a connector model in large-scale finite element explicit crash simulations. The NN model was established to describe the local force–deformation response of point connectors in automotive applications, namely self-piercing rivets and flow-drill-screws. The study is limited to two-sheet connections and to the use of feedforward NNs. Successive loading and unloading of the joints is not studied. Various architectures and complexities of the feedforward NNs were evaluated and trained based on data generated from a constraint model found in the literature. This forms a proof of concept for implementing a modelling technique not based on physics-motivated constitutive equations. The impact of the network complexity and training data diversity was investigated. The NN model was implemented as a cohesive zone model for incremental force prediction in an explicit finite element code. In order to have a wide selection of joint types, five different joint configurations including self-piercing rivets (SPR) and flow-drill screws (FDS) were investigated. Numerical results from the NN model were compared to physical tests from all joint configurations. It was shown that a rather basic machine learning technique like a feedforward NN was able to reproduce path-dependent force–deformation behaviour for the application in explicit FE solvers.

1. Introduction

Placing the right material in the needed position of a car body, in a plane fuselage or in a building structure is a key to a purposeful design. Structural joining of multi-material parts requires appropriate techniques and fastener types. In designs where welding is not possible because the materials are too dissimilar, other techniques like adhesive bonding and/or mechanical fasteners must be considered. Modelling of such joints for engineering purposes is a challenge, and an interdisciplinary research is necessary to understand the deformation behaviour including damage and fracture.

A combination of physical testing and numerical methods are normally used to investigate the joint behaviour, serving as a basis for large-scale predictions of a final product. The term large-scale simulations is hereby used for full car crash simulations. The investigated modelling techniques could be applied to these large scale simulations. In addition to quasi-static conditions, dynamic loadings are also commonly investigated for typical joints used in automotive applications [1]. In the design process of structures, finite element analyses with large shell elements are usually used in order to increase computational efficiency. This always means a trade-off between accuracy and computational time with respect to material modelling [2], for instance. Modelling the strength and ductility of mechanical fasteners, spot welds and structural adhesives is also subjected to the same constraints. These connections are traditionally represented by simplified models, see for instance Combescure et al. [3], Sønstabø et al. [4], Reil et al. [5], Porcaro et al. [6].

These simplified models are usually developed for specific joining techniques, see for instance the model proposed for SPR by Hanssen et al. [7], and must be carefully validated if applied to represent the behaviour for other techniques. Most of the models share common features like elasto-plastic force–displacement response under various loading mode mixities, loading/reloading and damage/failure. Marzi et al. [8] for example presented a rate-dependent cohesive zone model for modelling of structural adhesive. This model was applied by Bier et al. [9] for the large-scale modelling of spot weld connections, showing that some modelling techniques can also be applied to joining techniques where the model was not initially intended for. As per today, for every new joining technique a new simplified model has

* Corresponding author.
E-mail addresses: victor.andre@ntnu.no (V. André), miguel.costas@ntnu.no (M. Costas), magnus.langseth@ntnu.no (M. Langseth), david.morin@ntnu.no (D. Morin).

https://doi.org/10.1016/j.ijimpeng.2023.104490

Available online 28 January 2023

Nomenclature

d_n, d_t	Normal and tangential stretch
$\bar{\delta}_n$, $\bar{\delta}_t$	Normal and tangential stretch history
f_n, f_t	Normal and tangential force
$\hat{f}_n$, $\hat{f}_t$	Dimensionless normal and tangential force
$\hat{\boldsymbol{n}}_m$	Normal vector, master sheet
$\hat{\boldsymbol{n}}_s$	Normal vector, slave sheet
$\hat{\boldsymbol{n}}_o$	Out-of-plane normal vector
f_n^{max}	Maximum normal capacity, model parameter
f_t^{max}	Maximum tangential capacity, model parameter
i	Time step
t	Time
$\alpha_1, \alpha_2, \alpha_3$	Dimensionless model parameters
$\boldsymbol{\delta}$	Total stretch
δ_n, δ_t	Scalar value of normal and tangential stretch vector
δ_n^{fail}	Normal deformation at failure (pure normal loading)
δ_t^{fail}	Tangential deformation at failure (pure tangential loading)
η	Effective displacement measure
η_{max}	Maximum effective displacement measure, damage
θ	Loading direction
ξ_n	Dimensionless model parameter, defining softening region for normal loading
ξ_t	Dimensionless model parameter, defining softening region for tangential loading

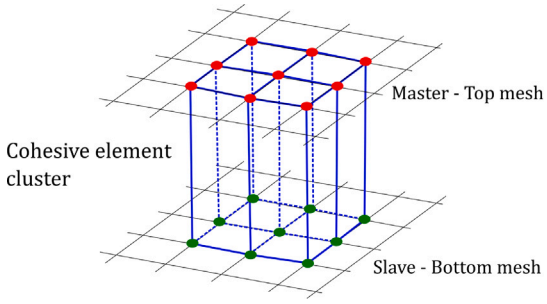

Fig. 1. Tied cluster of four cohesive elements between master and slave mesh.

to be developed or an existing one must be adapted and thoroughly validated. As the need for joining materials of dissimilar nature seems consistently increasing, the need for such simplified models is expected to grow as more and more joining techniques appear on the market.

According to Bonatti et al. [10], the modelling of materials and especially history-dependent mechanical behaviour has recently seen the advantage of machine learning methods. Bock et al. [11] states that machine learning tools empower material scientists and engineers to accelerate the development of new materials, processes and techniques. Burton et al. [12] brake down the application of machine learning into three areas in structural engineering. These areas are the improvement of empirical models, the surrogate modelling of expensive structural tasks, and information extraction methods. Both surrogate modelling and information extraction methods could be used to improve mechanical joint modelling techniques. Both in terms of modelling the physical joint behaviour in structural analyses as well as exploring the vast amount of potential joint-material combinations. Such an approach will give more flexibility for fitting of different joint types rather than having specific simplified models for each type of joint.

In the present study, a feedforward NN model was trained based on the point-connector model developed by Hanssen et al. [7]. The trained NN model was then implemented as a cohesive material subroutine in the commercial explicit solver LS-DYNA [13] for computing the force–displacement responses of the joints. The model by Hanssen was applied to self-piercing rivet (SPR) and flow-drill screw (FDS) connections. One SPR and four FDS joints characterised by Sønstabø et al. [4,14,15] were taken as experimental foundation and benchmark for the present work. The work of Sønstabø included joint characterisation with model parameter fitting, component testing and simulation. The applied workflow is briefly described as follows:

- Choosing five unique joint configurations.
- Creation of a training database for each joint model with parameters obtained by Sønstabø et al. [4,14–16]
- Training of various NN architectures and selection of one reliable design for all joints.
- Verification of NN models applied as a cohesive material model with single joint unit test/simulation.
- Validation of NN cohesive material model with complex component tests.
- Repetition of NN training with varying amount and quality of training data.
- Repetition of selected component simulation.

The data set generation and the NN training were done using Python and Keras packages [17], afterwards the trained weights were parsed to the user subroutine as parameters. While impact loadings are considered in this work, the rate sensitivity of the connections is neglected. For instance, the work of Porcaro et al. [18] showed no rate effects when aluminium sheets joined by self-piercing rivets were subjected to impact loadings. In this context the present paper aims at demonstrating the applicability of NNs to the modelling of joints in large-scale crash analyses. This work will then serve as a proof of concept and pave the way for future data-driven models dedicated to joints.

2. Modelling of joint behaviour

When using shells in large scale crash analyses, the modelling approach for connecting two mating sheets is realised by a connector element or a constraint model. In this paper the constraint model by Hanssen et al. [7] is applied. The governing equations of the model were used for training of the NN. Depending on the relative nodal deformations between the shells representing the sheets, the resulting force and moment components were calculated for various mode angles and loading/unloading cases. The model by Hanssen et al. [7] was initially intended for SPR connections, but Sønstabo et al. [16] showed that it could be successfully applied to FDS connections as well.

2.1. Constraint model introduction

In the model by Hansen et al. [7], a master and a slave sheet are defined, represented by master and slave node regions. The spatial relative deformation is decomposed into a normal and tangential part, where the normal direction is orthogonal to the sheets' mid-surface and the tangential direction is in-plane of the sheets.

The relative nodal displacements between the sheets are named stretches, and denoted δ_n (normal) and δ_t (tangential) stretch, respectively. The model takes those stretches as input variables and calculates a normal f_n and tangential force component f_t. The governing equations of the constraint model, which link forces and displacements, are given in Table 1. In addition to the force components, a damage variable named maximum effective displacement η_{max} is calculated. It evolves during joint deformation and depends on the loading mode. The damage variable indicates maximum joint opening and drives joint

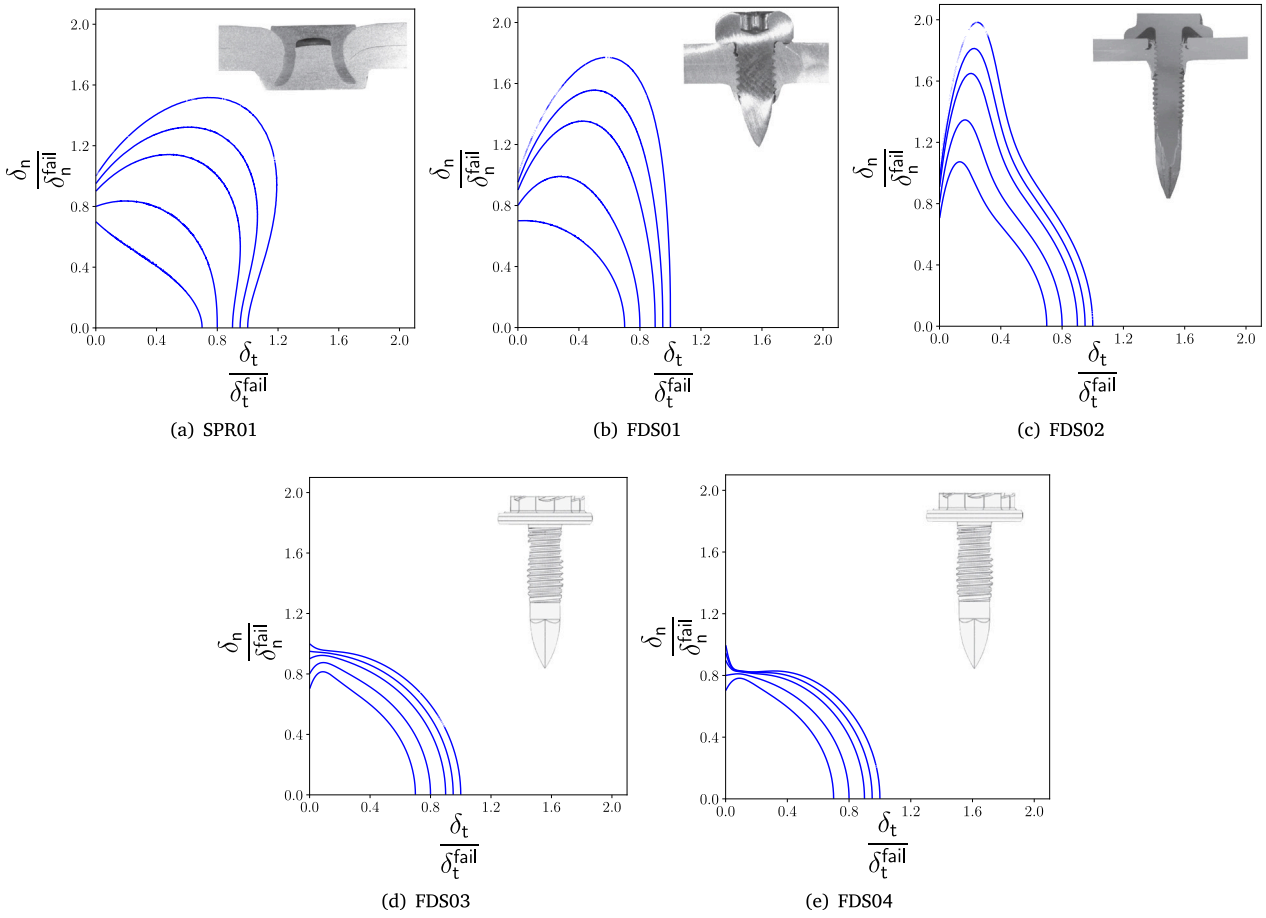

Fig. 2. Failure loci of investigated connections; maximum effective displacement levels [0.7, 0.8, 0.9, 0.95, 1.0].

Table 1
Constraint model, governing equations [7,16].

Total stretch $\boldsymbol{\delta}$ defined as the vector between slave end and original location on the deformed slave sheet. Normal and tangential stretch: $\boldsymbol{\delta} = \boldsymbol{\delta}_n + \boldsymbol{\delta}_t, \quad \delta_n = \lvert\boldsymbol{\delta}\cdot\hat{\boldsymbol{n}}_m\rvert, \quad \delta_t = \lvert\boldsymbol{\delta}\cdot\hat{\boldsymbol{n}}_t\rvert, \quad \hat{\boldsymbol{n}}_t = \hat{\boldsymbol{n}}_0 \times \hat{\boldsymbol{n}}_m$	Loading direction: $\theta = \arctan\left(\frac{\delta_t}{\delta_n}\right)$
Forces are calculated directly from mathematical expressions: $f_n = \frac{f_n^{max}\delta_n}{\eta_{max}\delta_n^{fail}}\hat{f}_n, \quad f_t = \frac{f_t^{max}\delta_t}{\eta_{max}\delta_t^{fail}}\hat{f}_t,$ where $\hat{f}_n = \begin{cases} 1-\left(\frac{\xi_n-\eta_{max}}{\xi_n}\right)^8, & \eta_{max} \le \xi_n \\ 1-\frac{\eta_{max}-\xi_n}{1-\xi_n}, & \eta_{max} > \xi_n \end{cases}$ $\hat{f}_t = \begin{cases} 1-\left(\frac{\xi_t-\eta_{max}}{\xi_t}\right)^8, & \eta_{max} \le \xi_t \\ 1-\frac{\eta_{max}-\xi_t}{1-\xi_t}, & \eta_{max} > \xi_t \end{cases}$ Exponent of 8 suggested by Hanssen et al. [7] but can be changed in the LSDYNA solvers.	Damage variables: $\eta = \left[\xi + \frac{1-\xi}{\alpha}\sqrt{\left(\frac{\delta_n}{\delta_n^{fail}}\right)^2 + \left(\frac{\delta_t}{\delta_t^{fail}}\right)^2}\right]$ $\xi = 1 - \frac{27}{4}\left(\frac{2\theta}{\pi}\right)^2 + \frac{27}{4}\left(\frac{2\theta}{\pi}\right)^3$ $\alpha = \begin{cases} \frac{\xi_t-\eta_{max}}{\eta_t}\alpha_1 + \frac{\eta_{max}}{\eta_t}\alpha_2, & \eta_{max} < \xi_t \\ \frac{1-\eta_{max}}{1-\xi_t}\alpha_2 + \frac{\eta_{max}-\xi_t}{1-\xi_t}\alpha_3, & \eta_{max} \ge \xi_t \end{cases}$

deletion. The model needs nine parameters which are found by inverse engineering of experimental tests in different loading directions. The moment acting on the master and slave sheets is calculated based on the force component and the sheet thicknesses. The models do allow for twisting around the fastener axis, as connections like SPR and FDS show neglectable twisting resistance.

In this work the governing equations from the constraint model were implemented as a cohesive material model applied to a cluster of cohesive elements representing the joint. This gives more freedom when modifying the force–displacement relationship and makes it possible to implement the NN model as a user subroutine. The force components and moments are transferred to the master and slave sheets via the cohesive element which is placed between both sheets, as seen in Fig. 1. When a critical value of damage is reached, the cohesive element gets eroded and no more joint forces will be transmitted to the previously connected sheet mesh. The nodes of the cohesive elements stay connected to the sheet mesh.

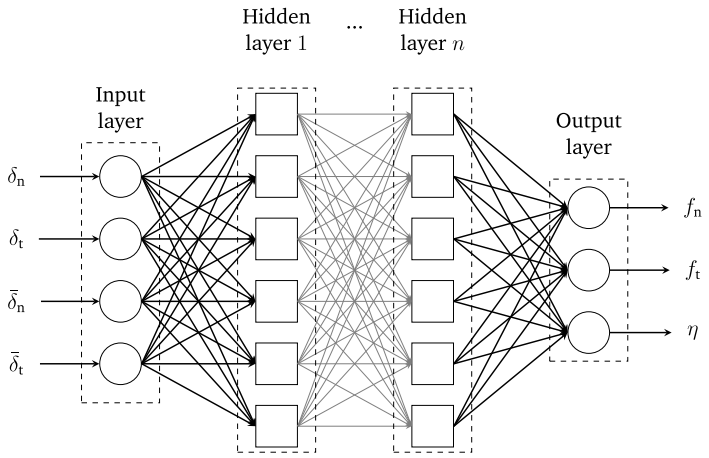

Fig. 3. Fully connected NN with four input variables (δ_n, δ_t, $\bar{\delta}_n$, $\bar{\delta}_t$) and three output variables (f_n, f_t, η).

2.2. Investigated joints

Five unique joint configurations were investigated in order to challenge the versatility of the NN modelling approach. Those five joints are characterised by the joined material pairing and the fastener type, marked with an ID for later reference:

- SPR01: a SPR connection between two rolled aluminium sheets made from AA6016 T4 each 2 mm thick. The rivet has an overall length of 6.5 mm with a shank diameter of 5 mm.
- FDS01: a small screw FDS connection between two rolled aluminium sheets made from AA6016 T4 each 2 mm thick (similar to SPR01). The screw has an overall length of 13 mm with a thread diameter of 4 mm and a head diameter of 8 mm.
- FDS02: a large screw FDS connection between two rolled aluminium sheets made from AA6016 T4 (top sheet) and AA6063 T6 (bottom sheet) each 2 mm thick. The screw has an overall length of 25 mm with a shank diameter of 5 mm and a head diameter of 14.4 mm.
- FDS03: a large screw FDS connection between two extruded aluminium profiles made from AA6060 T6 each 2.5 mm thick. The screw has an overall length of 24 mm with a thread diameter of 5 mm and a head diameter of 13 mm.
- FDS04: a large screw FDS connection between two extruded aluminium profiles made from AA6060 T6 (top) and AA6005 T6 (bottom) each 2.5 mm thick. The screw used in FDS04 was the same as in connection FDS03.

The failure loci, obtained from the constraint model, of the investigated joints is shown in Fig. 2. The figure shows how the maximum effective displacement (damage) evolves with increased stretch. The failure surface has a different shape for each joint and one can see for example how the maximum displacement is increased for mixed mode loading for joint SPR01 and FDS01, compared to pure normal or shear. On the other hand, joint FDS02 shows an increased maximum displacement under normal loading mode. FDS03 and FDS04 show a similarly shaped failure loci as they both use the same fastener type, same material thickness but different material.

3. Neural network representation

The described constraint model was mimicked by a feedforward neural network (NN). For a given deformation state, the network should predict the corresponding force components and the damage variable. The NN is not able to capture unloading and cyclic loading as it only takes stretch components as input variables. The NN does not memorise if it already had made a prediction on a given input set. A prediction on the same stretch input would always yield the corresponding force output, no matter if the previously fed stretch input was different. The NN does not distinguish between rising or decreasing stretch paths. Therefore for the NN to be able to capture cyclic loading, two additional input variables were introduced in order to increase the network dimension from 2 to 4 and to capture the path-dependent behaviour. In addition to the normal δ_n and tangential stretch δ_t, a history measure for each stretch component is calculated. Those history variables are denoted $\bar{\delta}_n$ and $\bar{\delta}_t$. The way of calculating the history of stretch is inspired and abstracted from Gorji et al. [19]. The measure is realised by incrementally calculating a running mean measure of the stretch component (see Table 2). The stretch history is only dependent on the current stretch input and the running mean of the previous stretches. Previous force outputs are not used as history values so that a prediction error is not propagated to the input variables which would result in an error accumulation over multiple iterations.

Table 2
History measure for NN input variables.

Analytical stretch measure for normal and tangential stretch over deformation time t:
$\bar{\delta}_n = \frac{1}{t}\int_0^t \delta_n(t)\,\mathrm{d}t, \quad \bar{\delta}_t = \frac{1}{t}\int_0^t \delta_t(t)\,\mathrm{d}t$
Incremental stretch measure calculation over time step i:
$\bar{\delta}_n^i = \bar{\delta}_n^{i-1} + \frac{\delta_n^i - \bar{\delta}_n^{i-1}}{i}, \quad \bar{\delta}_t^i = \bar{\delta}_t^{i-1} + \frac{\delta_t^i - \bar{\delta}_t^{i-1}}{i}$

A generic NN architecture with input and output variables is displayed in Fig. 3. The desired NN design should give a reasonable representation of the problem without over- or underfitting, while keeping the number of nodes and layers to a minimum in order to reduce computational cost. In order to find this reliable NN design, the number of hidden layers n and the number of nodes per hidden layer was varied with a maximum of four hidden layers and 500 nodes per hidden layer. The nodes contained in a hidden layer are called hidden nodes for later reference. The effect of network architecture on the goodness of the fit is presented in Section 3.3. The network training was carried out using an adaptive gradient descend method, namely the Nesterov-accelerated Adaptive Moment Estimation [20]. The objective function was the mean squared error (MSE) between the network prediction $\bar{y}$ and the given target value y. The MSE represents the quantitative deviation between training targets and the network prediction during training. All hidden layers were activated with the Leaky rectified linear unit function (LeakyReLU), enforcing a positive gradient even for negative inputs. The problem with the general rectified linear unit is the zero gradient for negative input values. When applying the back-propagation process during training, that zero gradient would

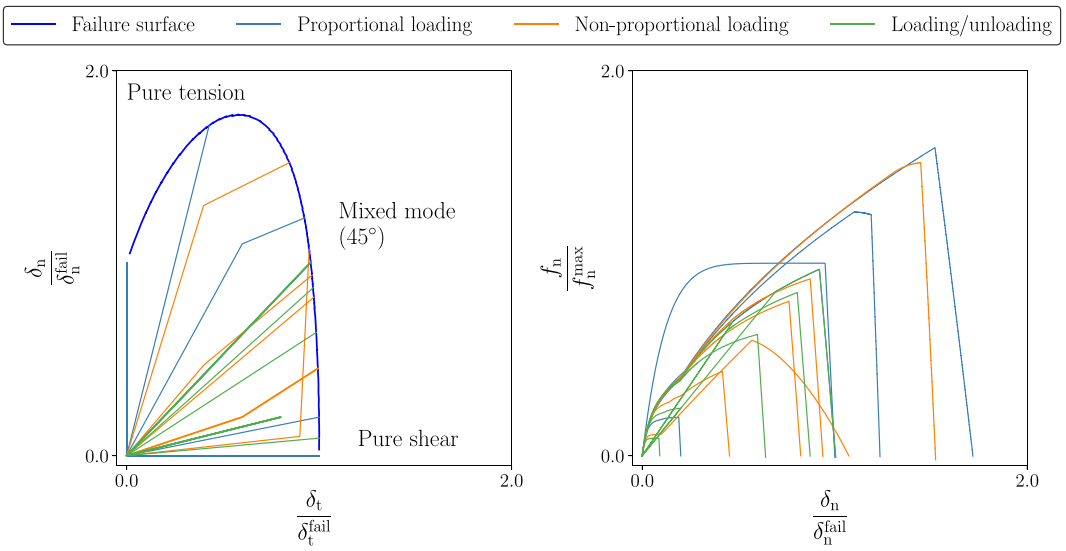

Fig. 4. Exemplary training paths in stretch space and corresponding normal force-stretch response.

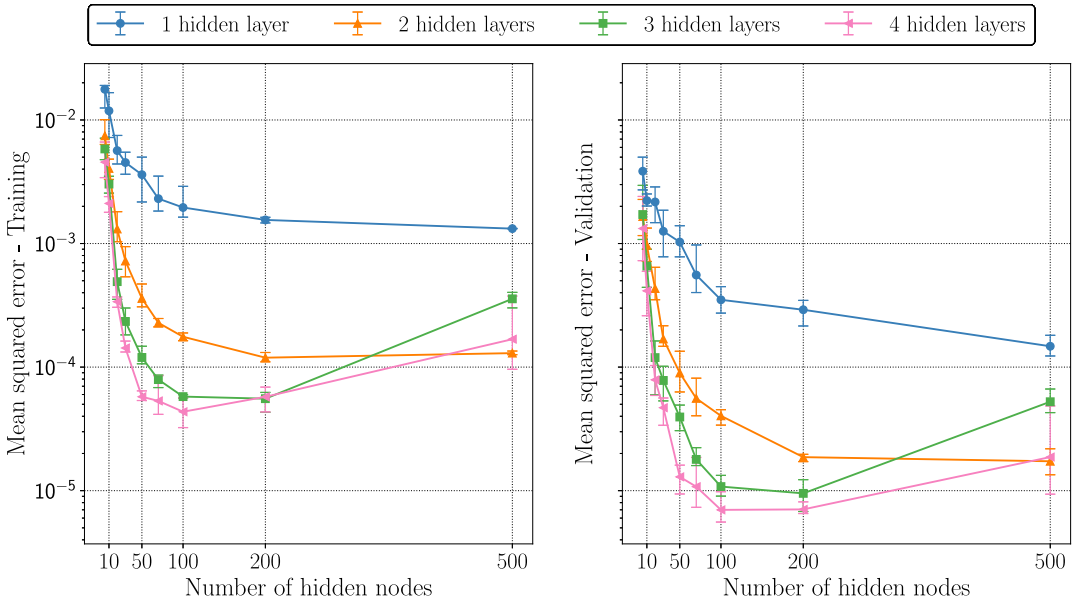

Fig. 5. Final training (left) and validation (right) MSE for joint FDS01; error bar shows the highest, lowest and mean achieved final MSE.

stop the adjustment of the respective neurons weights. The LeakyReLU function gives a slight positive gradient for negative input values and therefore overcomes the problem of vanishing gradient,as shown by Glorot et al. [21]. The NN and Hanssen model do not account for joint compression, as compression of the joint area is constrained by the contact formulation between sheets. Therefore, the output layer is activated with ReLU to give strictly positive values, just like the constraint model.

3.1. Virtual data creation

The training data for fitting the NN was directly generated using the constraint model described in Section 2.1. The input variables fed to the constraint model were stretch paths. The stretch paths corresponded to loading a joint from a virgin state to failure, including non-proportional loading and unloading. If one or both of the stretch components decreases, the model experiences unloading with a decrease of force while η_{max} remains constant, storing the maximum occurred value.

An output variable should not dominate others in magnitude when using gradient based optimisation methods. Thus, the NN was trained on normalised data. The stretch components and their corresponding history measures should be scaled down by their maximum occurring value. In this case, they were scaled by the model parameters δ_n^{fail} and δ_t^{fail}, which are not the maximum occurring values but still in the higher range. The force components were scaled respectively by f_n^{max} and f_t^{max}. Scaling of input and output values improved the NN training since it brought the magnitudes of the gradient closer together [22]. For example the target error of the normal force component f_n should have the same impact on the optimisation algorithm as a target error of η, as all output variables are equally important.

3.2. Load case definition

A NN can make predictions on any input value, but it only gives reasonable predictions on data it has seen before. This is called supervised training, with the typical application of the present regression task. A sufficient representation of the input variable space with the

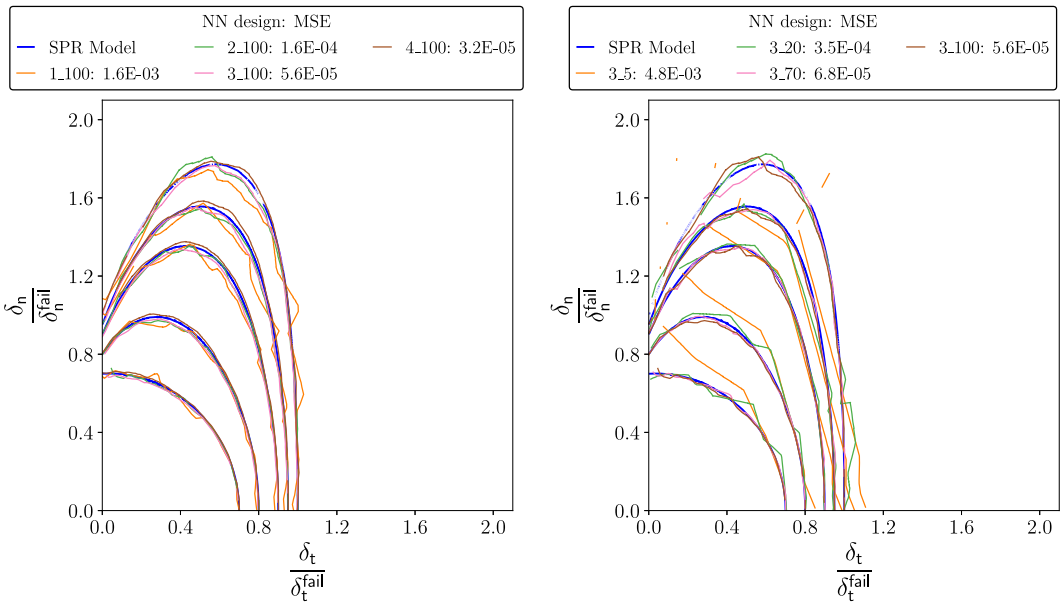

Fig. 6. Contour plots with equal max. effective displacement values; η_{max} = [0.7, 0.8, 0.9, 0.95, 1.0], radially increasing.

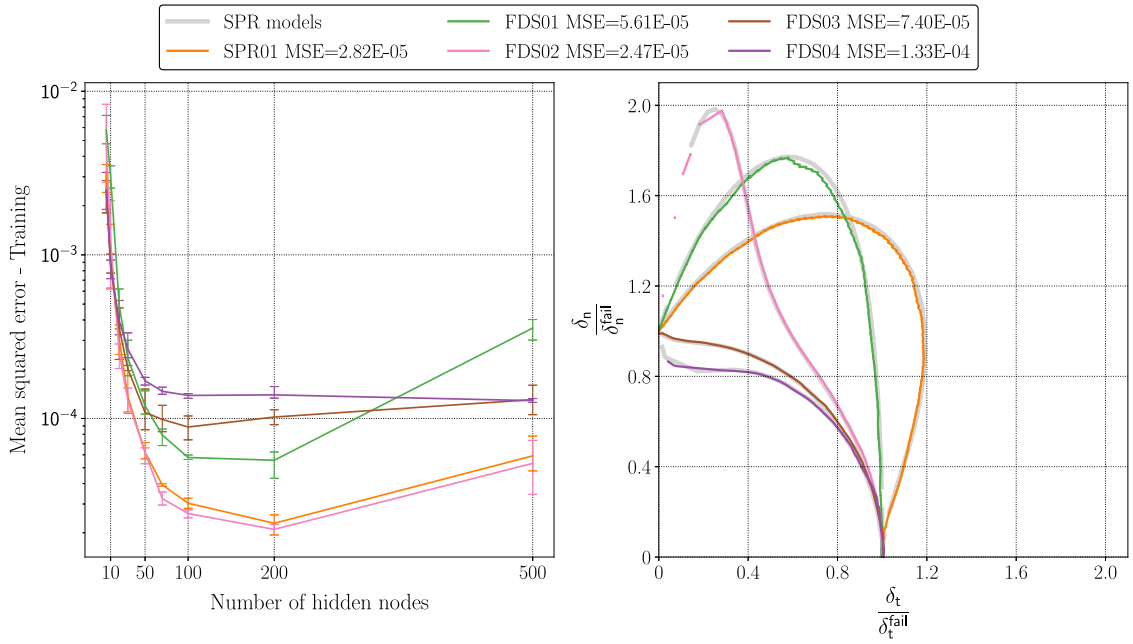

Fig. 7. Training MSE versus number of hidden nodes in three hidden layers (left); predicted failure loci for all joints with respective 3_100 NN model.

corresponding output is necessary to train any NN. Since the joint can experience infinite loading modes and unloading scenarios, a NN capable of working under any scenario was targeted. A more dense mapping of loading modes would probably result in better prediction capabilities, but it would also increase the amount of training data needed. In order to determine how complex the training set should be for a reliable representation, the networks were trained on three different data sets, with an increasing level of complexity:

- Proportional loading with a steady loading mode/angle.
- Non-proportional loading (e.g. diverging from pure shear into mixed).
- Unloading and reloading of the joint.

Prediction of the stretch-force response and the damage evolution are critical since both features have direct influence on the global deformation behaviour of a joined component. Fig. 4 shows exemplary training cases with various modes in the stretch space, non-proportional loading and unloading. While the figure is only symbolising the training database creation, the actual database used for the NN training consisted of ca. 1000 paths with much finer mode discretisation.

3.3. Network architecture

The ability of a NN to output reliable predictions strongly depends on the general architecture in terms of the number of hidden layers and hidden nodes. In general, more layers and neurons give a better fit to more complex and higher dimensional problems. Nevertheless, it was shown by Fahlman et al. [23] and Nakama [24] that a higher number of layers is not always better. Not only does it increase the number of trainable weights, but gradient based training can become ineffective

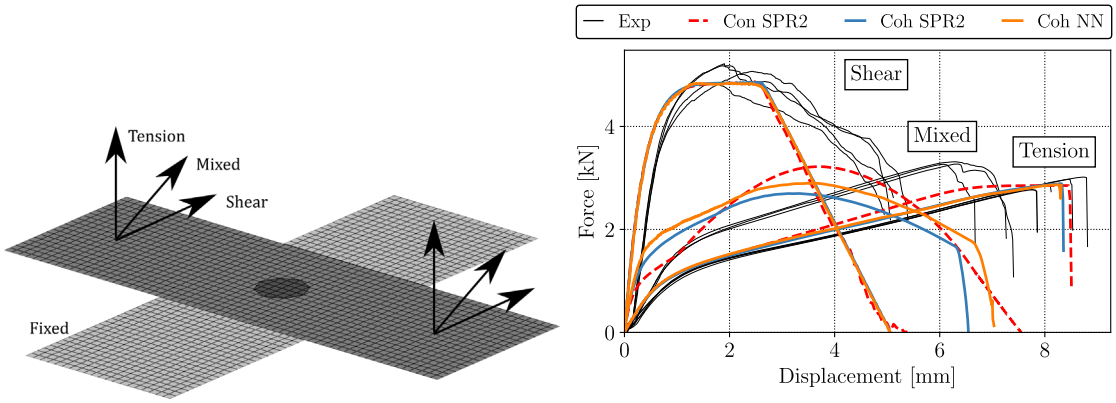

(a) Cross test mesh (b) Legend: Con-Constraint, Coh-Cohesive element

Fig. 8. Cross test mesh (a) and results from FDS01 simulation (b).

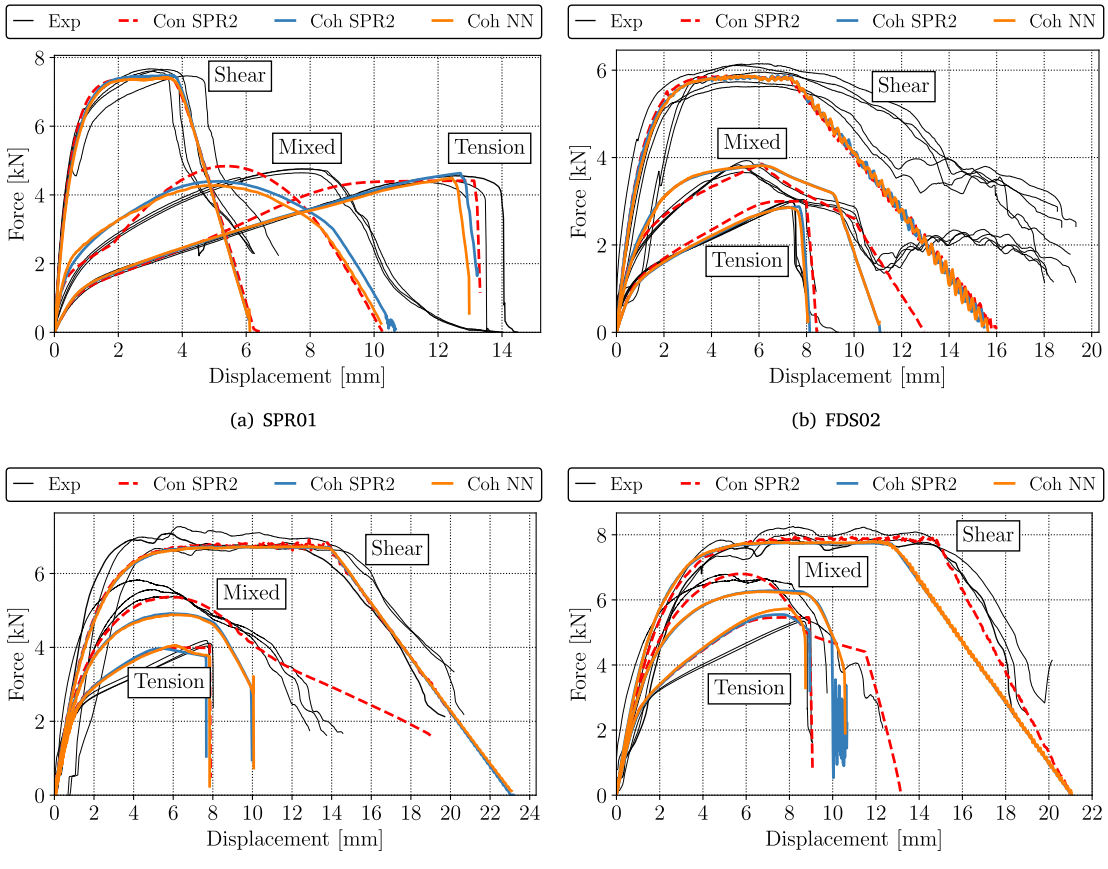

(a) SPR01 (b) FDS02

(c) FDS03 (d) FDS04

Fig. 9. Cross test simulations; Legend: Con-Constraint, Coh-Cohesive element.

because of the vanishing gradient problem in the back-propagation process. NNs with high dimensionality can also lead to overfitting of the task.

In order to find a feasible combination of hidden layer amount and nodes per hidden layer, a full factorial design of experiments was set up and the performance of the various architectures was evaluated. With the combination of one to four hidden layers and each layer having 5, 10, 20, 30, 50, 70, 100, 200 or 500 nodes, the full factorial design resulted in 36 different architectures. The amount of nodes per hidden layer was kept equal for every hidden layer. The NNs performance was evaluated based on the MSE of the training set and of a separate validation set. Each network design was trained until the MSE converged.

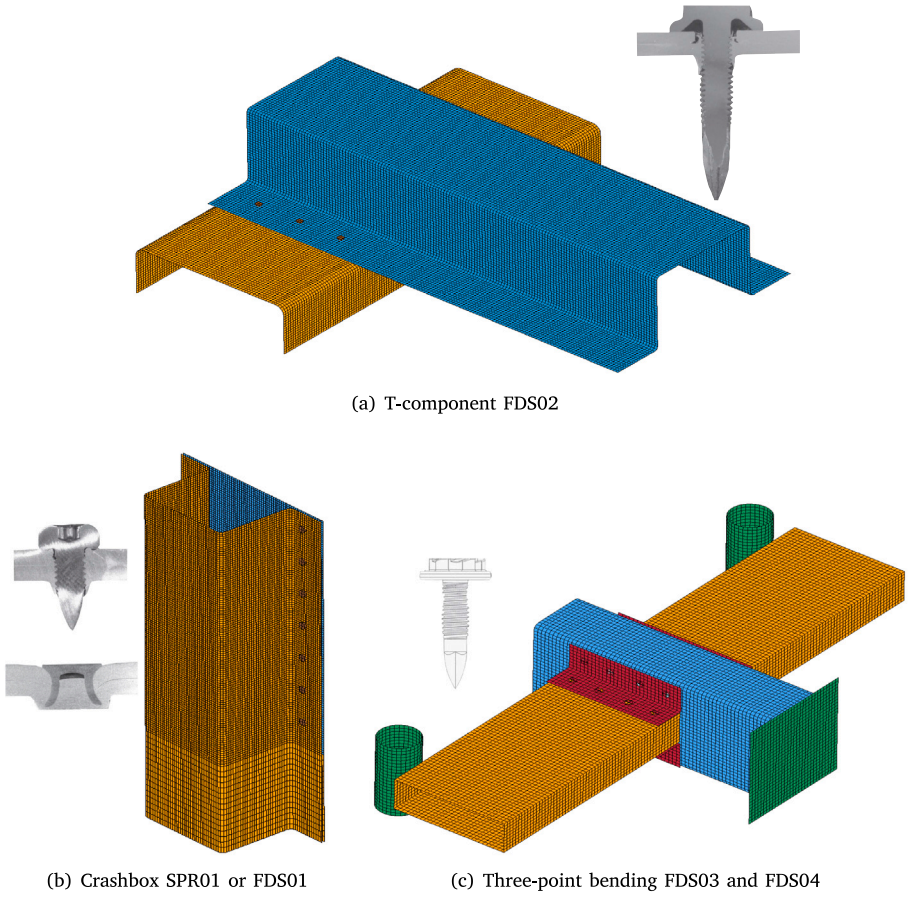

(a) T-component FDS02

(b) Crashbox SPR01 or FDS01

(c) Three-point bending FDS03 and FDS04

Fig. 10. FE mesh for component tests.

The training data basis was equal for each joint consisting of stretch paths and the corresponding history measures. The training data was a combination of all three loading scenarios described in Section 3.2; called a fully trained network. That results in 50 proportional loading paths, 20 load paths with each having 20 unloading points and 200 non-proportional loading paths. Additional validation data was created which is not seen by the network during training. That validation set is a collection of non-proportional loading paths with two points of mode change and full unloading or failure. The validation data set is meant to describe an even more complex loading scenario than the one given during training. The same training and validation set was used while the network design was changed.

The training data was split into 80 % for training and 20 % for testing. Each load path consisted of approximately 500–1000 increments which build up one training sample. The data was split randomly among those samples with the given train/test-ratio. Each network design was trained with different weight initialisation for five repetitions to account for the effect of network initialisation and variance of MSE. Both the finally achieved training and the validation MSE are displayed in Fig. 5 as a result of the chosen network design for joint FDS01. NN training duration was between 50 and 250 epochs until convergence. A reduction of the final training error by a factor of 10 could be seen when two instead of one hidden layer were used. The use of a fourth hidden layer gave marginal improvement over the use of only three hidden layers. The network performance with designs of 200 and 500 hidden nodes seemed to decrease, probably because the training duration was not long enough in order to fit the higher dimension network. Higher order NNs seemed to need more training epochs in order to achieve final error convergence. Fig. 6 shows the damage loci with contour lines at equal maximum effective displacement for proportional loading. The nomenclature for distinguishing between NN designs is denoted h_n with h and n being the number of hidden layers and the amount of nodes per hidden layer, respectively. The corresponding MSE for each NN design is taken from the full training which included all three training scenarios. One can see that all designs with 100 hidden nodes give reasonable damage loci prediction, where the most complex design with four hidden layers performed best. On the other hand, when three hidden layers were fixed and the number of hidden nodes altered, the results with five and 20 hidden nodes were poor, especially for higher damage levels.

The same trend of low MSE with higher NN complexity could be seen for the other investigated joint types in Fig. 7. A NN design with three hidden layers and 100 nodes seemed to be a good choice for modelling all joints without having too many trainable weights. It should be noted how different the shapes of the failure loci are and how the architecture is flexible enough to account for that. Therefore the design 3_100 was employed for the next validation steps.

4. Single connector test and component validation

The NN models from Section 3.3 were applied in large-scale FEM analysis and verified against single connector tests, so called cross tests. Those cross test have been used by Sønstabø et al. [4,14–16] for fitting the constraint model parameters. The same parameters where used for

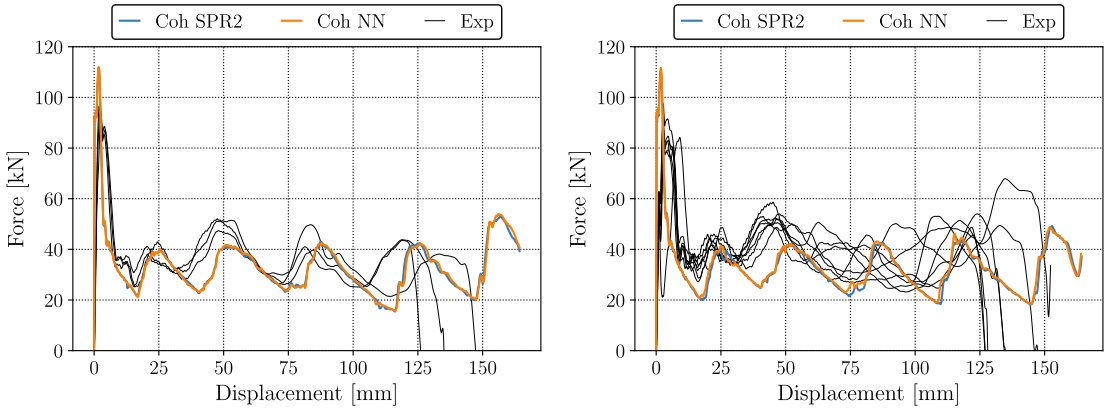

(a) Global response FDS01

(b) Global response SPR01

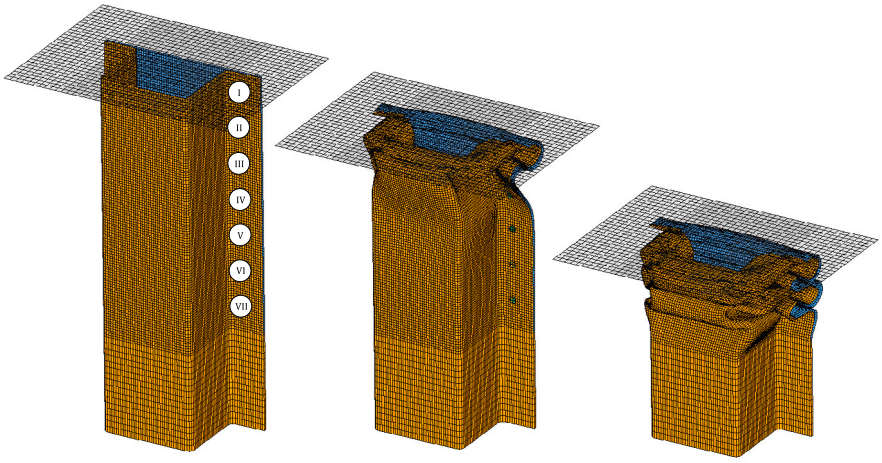

(c) Development of buckling during crushing with labelling of cohesive element position

Fig. 11. Results from dynamic axial crushing simulation FDS01 and SPR01.

the cohesive elements applying the Hanssen model and to train the NN models. In addition, the NN models were validated with complex component simulations and compared to the model by Hanssen et al. [7] applied to cohesive elements. The component tests were designed to challenge each of the investigated joints. In order to validate the NN models the global force–displacement response and the local response in the cohesive elements were compared.

4.1. Cross test and NN verification

The parameters for the constraint model can be found by inverse modelling of a cross test. A cross test consists of two overlapping sheets with the joint in the centre, shown in Fig. 8(a). The sheets are rotated 90° with respect to each other so that they can be clamped in a test machine. The two sheets are then pulled apart in a tension, shear and mixed mode. The constraint model parameters for the investigated joints were found by Sønstabø et al. [4,14–16] and are given in Table A.3.

The cross test simulations were set up in three ways: with the constraint model by Hanssen et al. [7], a cluster of four cohesive elements replicating the constraint model, and four cohesive elements applying the fully trained 3_100 NN model. Four cohesive elements where used in order to give a better discretisation of the rivet area. The constraint model itself is applied in form of a node-to-node connection using the LS-DYNA keyword *CONSTRAINED_SPR2. The force–displacement response of the joint FDS01 is displayed in Fig. 8. It can be observed that the NN response is in good agreement with the constraint model under tension and shear mode. Under mixed mode loading, the NN approach showed approximately 10 % higher force and failure at higher displacement.

The cross test results for the remaining joints can be seen in Fig. 9. Good agreement between the NN and the Hanssen model applied to cohesive elements was found. All five cross test simulations showed a successful application of the NN model.

4.2. FE modelling

Fig. 10 shows the FE models used for validation with the component tests. Validation of joints SPR01 and FDS01 was done with a crash box model which was rigidly fixed at the bottom and axially crushed, Fig. 10(b). The T-component test, Fig. 10(a), was used for FDS02, where a hat-shaped part was pulled perpendicular to the U-shaped part resulting in a shear-dominated loading of the joints. Joints FDS03 and FDS04 were combined in the three-point-bending test, Fig. 10(c), where a double-chamber profile was pushed while two outer beams rested on rigid posts. All FE simulations were conducted in LS-DYNA with the explicit solver in its version 9.3.1 [13]. The plates were represented by a shell mesh using Belytshko–Tsay elements with reduced integration and five integration points through the thickness. The elements had a quadrilateral shape and an approximate size of 2×2 mm which is similar to mesh-sizes used in full car crash analyses. Friction between parts was modelled by a penalty-based formulation with a general friction coefficient of 0.2. In order to account for the work hardening in the bent parts of the cold-formed profiles, the initial plastic strain resulting

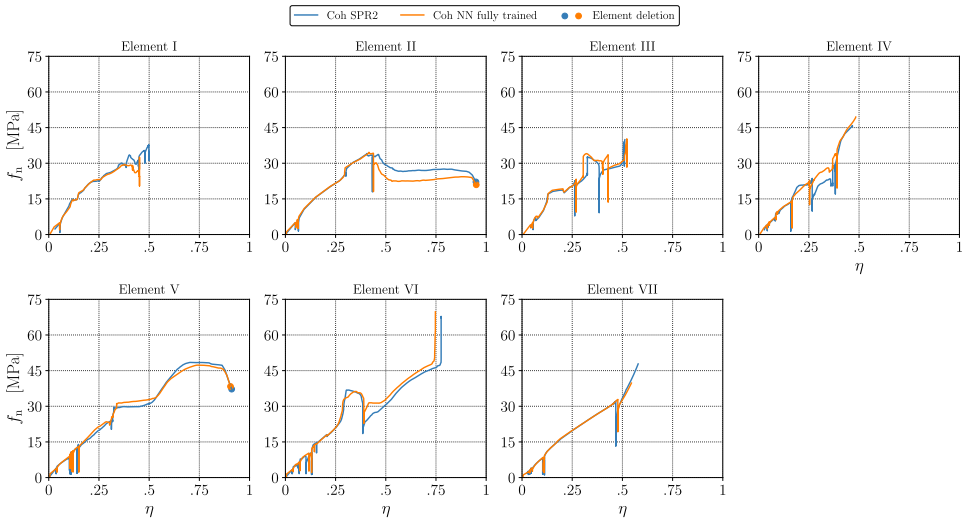

(a) Normal force f_n versus maximum effective displacement η

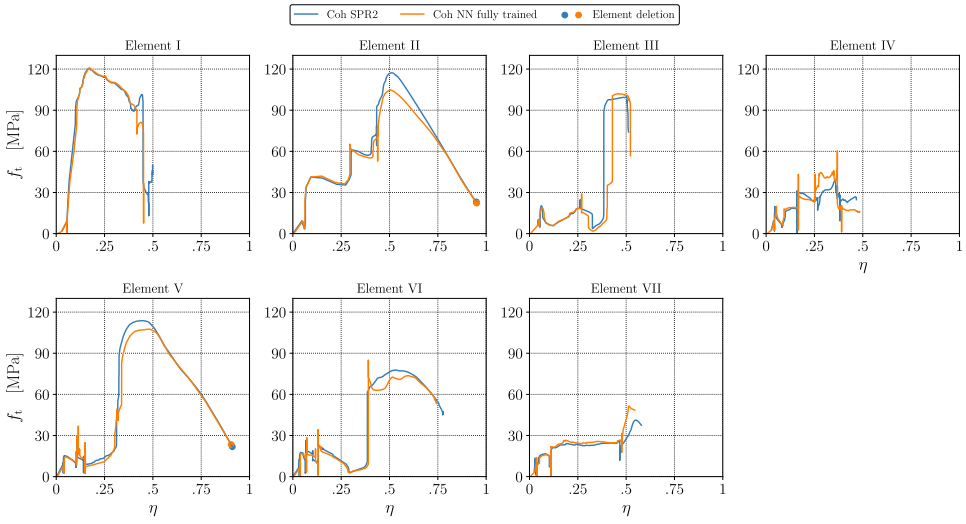

(b) Tangential force f_t versus maximum effective displacement η

Fig. 12. Local response from cohesive element FDS01; force normalised by cohesive element area.

from deformation was included in the models. All plates which were connected by joints were made from aluminium. An isotropic plasticity model was used for the plate material and the material parameters were adopted from Sønstabø et al. [4,14–16]. Governing equations and the respective material parameters can be found in Appendix A, Table A.4.

4.3. Component validation

The NN model was applied in a component simulation for each of the investigated joints. The performance of the cohesive elements applying the NN model was compared to cohesive elements applying the model by Hanssen et al. [7] (see Section 2.1) and related to the experimental results.

4.3.1. Crash box test with FDS01/SPR01

Fig. 11 shows the global force–displacement response from a dynamic axial crushing simulation for joint FDS01 and SPR01. The component experienced buckling and characteristic folding patterns (Fig. 11(c)) with a total crushing displacement of approximately 150 mm. The simulations were able to reproduce the deformation seen in the experiments, both with the model by Hanssen and the NN-model. Buckling of the profile was governing the force–displacement response so individual joint failure could not be assessed.

The local response from each of the cohesive elements resembling the seven joints is compared in Fig. 12. Each graph shows the evolution of the normal or tangential stress over the maximum effective displacement during axial crushing. Element deletion was initiated in elements II and V (see Fig. 11(c)) when reaching an effective maximum displacement $\eta = 1$. It is worth noticing that the effective maximum displacement cannot decrease as the value describes the amount of damage accumulated. A sudden decrease in stress without decreasing the effective maximum displacement implies unloading. The local behaviour is complex with multiple points of unloading and eventual failure with multiple changes of loading mode. The NN model was able to reproduce the force–deformation behaviour in many loading scenarios with relatively small stress deviation compared to the constraint model.

The crash box component was made from a hat-section profile and a flat plate joined with 14 rivets (seven per side) along the seam line. Symmetry was applied to reduce simulation time. The component was fixed at one end using rigid boundary conditions. The full-size component was subjected to an impacting mass of 395.5 kg at 10 m/s.

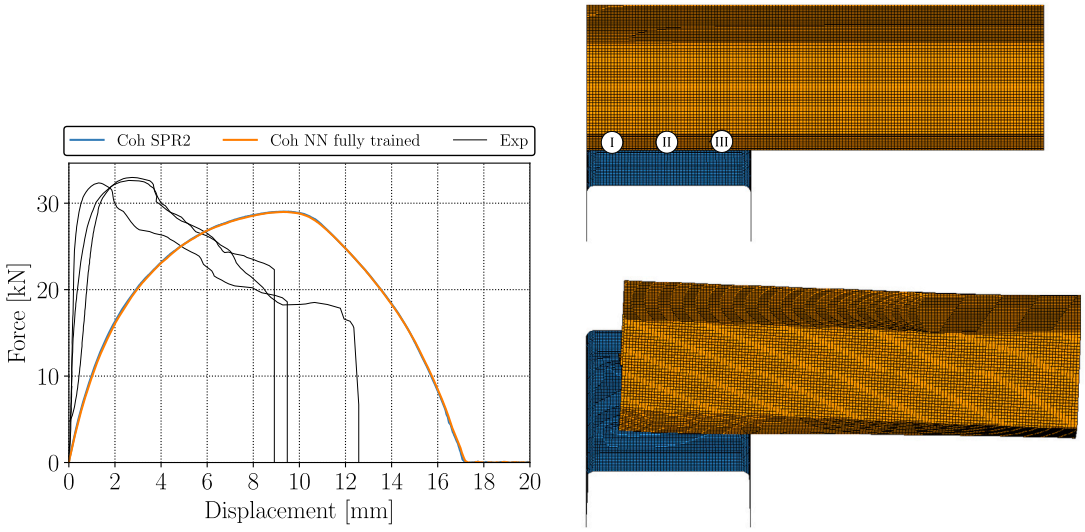

(a) Global force–displacement response

(b) Development of shear deformation with labelling of cohesive element position

Fig. 13. Result from T-component simulations FDS02.

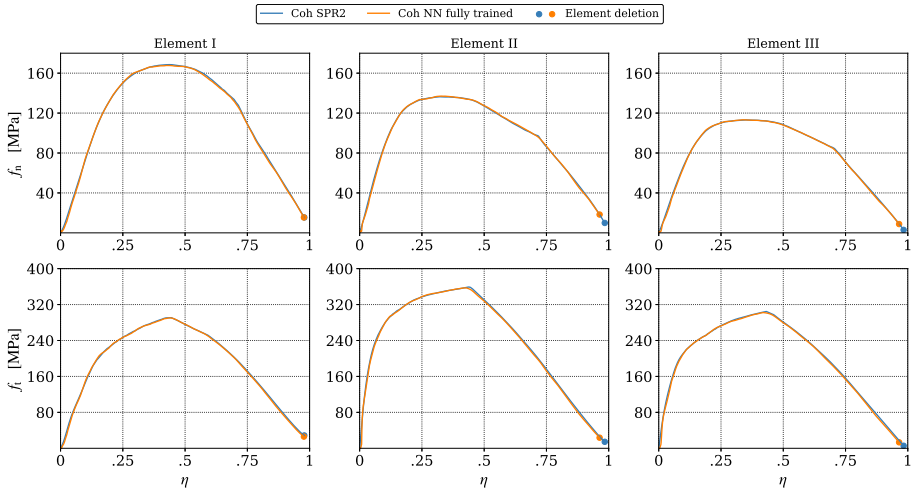

Fig. 14. Normal force f_n (top) and tangential force f_t (bottom) versus effective displacement η; forces normalised by cohesive element area.

The NN model was able to reproduce the local stress versus effective maximum displacement behaviour compared to the Hansen-model. The local response for the SPR01 simulation can be found in Appendix B Fig. B.27 and Fig. B.28.

4.3.2. T-component with FDS02

The global force–displacement response from the quasi-static T-component tests with joint FDS02 is displayed in Fig. 13(a). The specimen was composed of one U-shaped profile and one hat-section profile aligned at a 90° angle. The profiles were joined with three FDS on each side. The U-shape profile was clamped at both ends while the hat-profile was pulled axially at the free end, giving shear-dominated loading on the joints. Boundary conditions along the symmetry plane where applied to save computational cost. While the initial stiffness and shape of force–displacement curve of the experiments was not captured by the simulation, the NN-model gave exactly the same response as the constraint model it was trained on. The local stress versus effective maximum displacement response from the cohesive elements is seen in Fig. 14, where the NN-model copies the constraint model again.

4.3.3. Three-point bending test with FDS03/FDS04

Fig. 15 shows the global force–displacement response from the quasi-static three-point bending test for joints FDS03 and FDS04. The specimen consisted of an extruded double-chamber profile and two rectangular profiles attached in a 90° angle with L-brackets. The FDS03 joint was applied between the L-brackets and the rectangular profiles whereas the FDS04 joint was applied between the L-brackets and the double-chamber profile. The rectangular profiles rested on rigid posts and the double-chamber profile was axially loaded resulting in three-point bending. Joint failure of FDS04 could be seen between the L-brackets and the double-chamber profile. No deviation in stiffness could be seen between the constraint and the NN model in the beginning of the test due to deformation in the parts only. The sudden failure of elements IV and III was captured by both models, and is in good accordance with the experimental force drop. The NN model led to a sudden failure of elements II and III whereas the constraint model gave failure of the remaining joints at later point. The local stress versus the effective maximum displacement in the cohesive elements can be seen in Fig. 16 and in Fig. 17. The local response for joint FDS03 shows minor deviation between the constraint and the NN model. Both models

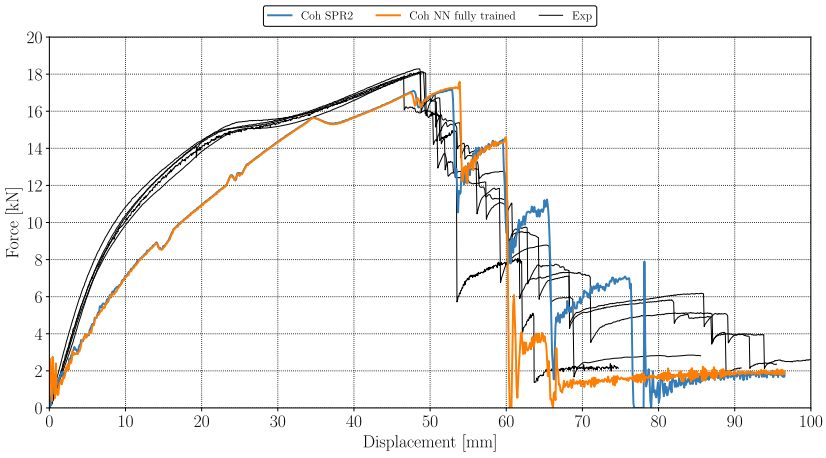

(a) Global force-displacement simulation (joint FDS03 and FDS04) compared to experiments

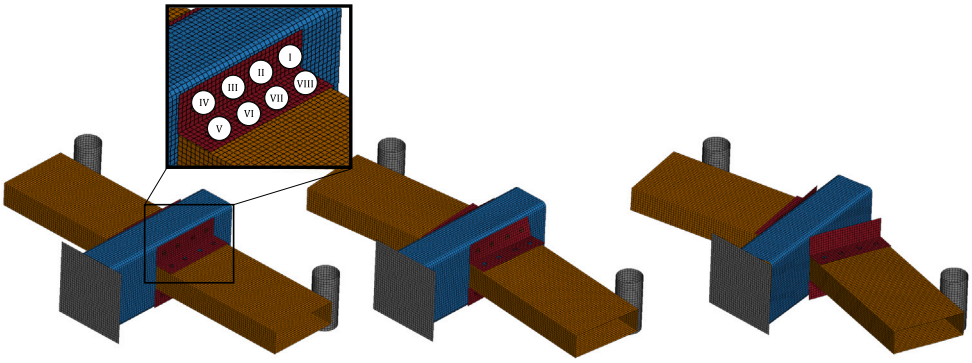

(b) Deformation pattern with labelling of cohesive element position

Fig. 15. Result from three-point bending simulation.

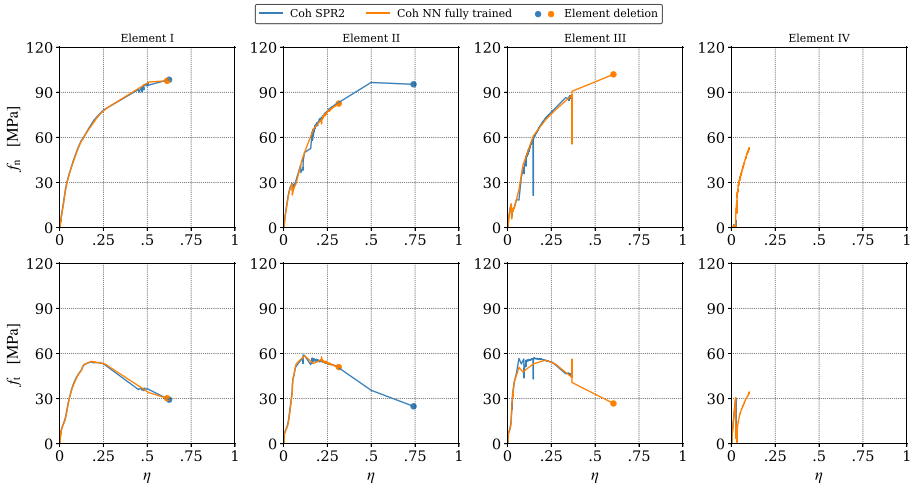

Fig. 16. FDS04: Normal force f_n (top) and tangential force f_t (bottom) versus maximum effective displacement η; forces normalised by cohesive element area.

were only challenged to an effective maximum displacement of 0.1. The deviation between the constraint and NN-model was relatively small for element I with an equal stress-response and point of failure. Elements II and III showed a good match of stress response but a premature failure of the NN model. Element IV showed no deviation between both models keeping in mind that the joints were only challenged until an early stage.

It was shown that a feedforward NN applied to a cohesive element could model the joints in the component and they performed well compared the cohesive elements applying the model by Hanssen. The local response showed how the NN model reproduces the model by Hanssen which served as the training basis. A common network architecture for all examined joints was found. With a large enough amount of training data, the NN model could probably replicate the constraint model even better.

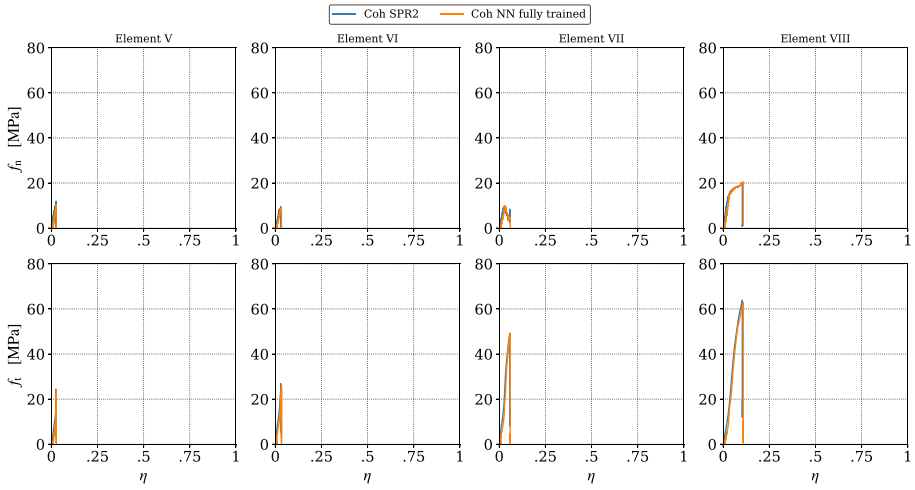

Fig. 17. FDS03: Normal force f_n (top) and tangential force f_t (bottom) versus maximum effective displacement η; forces normalised by cohesive element area.

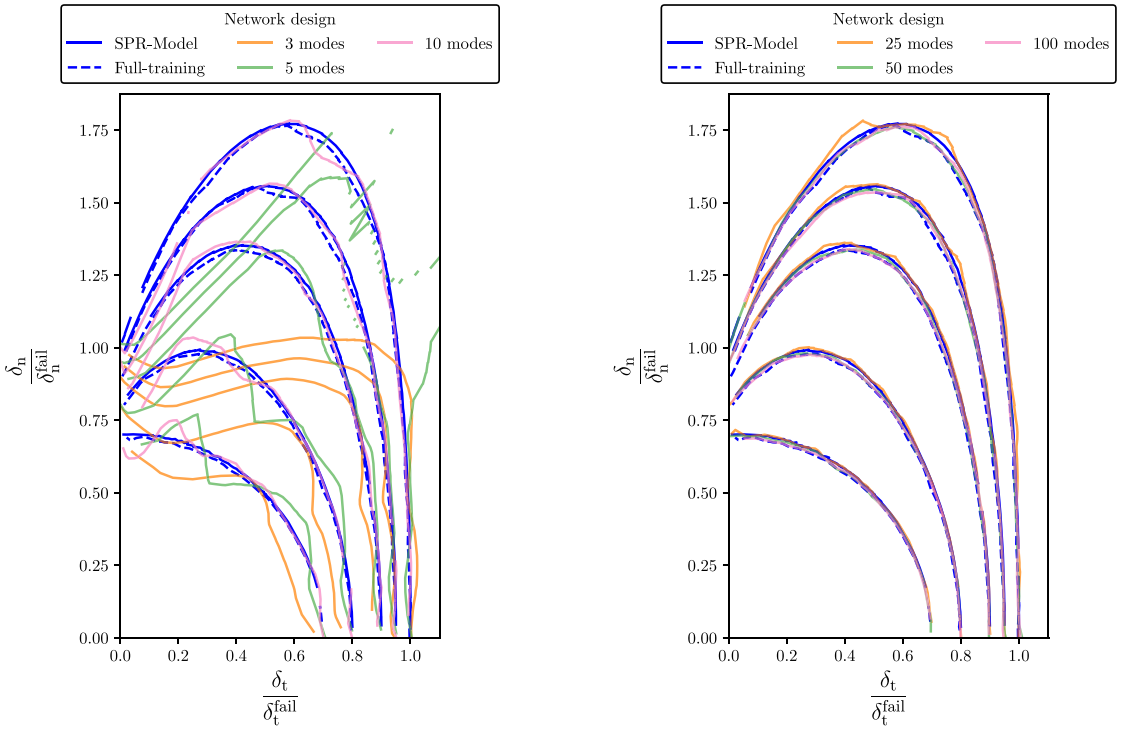

Fig. 18. Failure loci for NN trained on proportional loading with various amounts of modes, maximum effective displacement levels [0.7, 0.8, 0.9, 0.95, 1.0], joint FDS01.

5. Effects of partial training

This section covers the effect of data set size and data quality on the NN modelling. That means in particular the investigation on how many and which shape of stretch paths are necessary as training data in order to achieve a reasonable joint model. The amount of training paths necessary for a reasonable joint modelling will now be presented. The training scenarios from Section 3.2 were used in order to train a NN with a fixed 3_100 architecture but with various amounts of training paths. In order to study the effects of training amount, joints FDS01 and FDS04 were modelled with a reduced number of training paths and their respective component simulations were repeated. In Section 5.1 the effects of the three training scenarios (see Section 3.2) will be presented in detail with joint response predictions on virtual stretch paths.

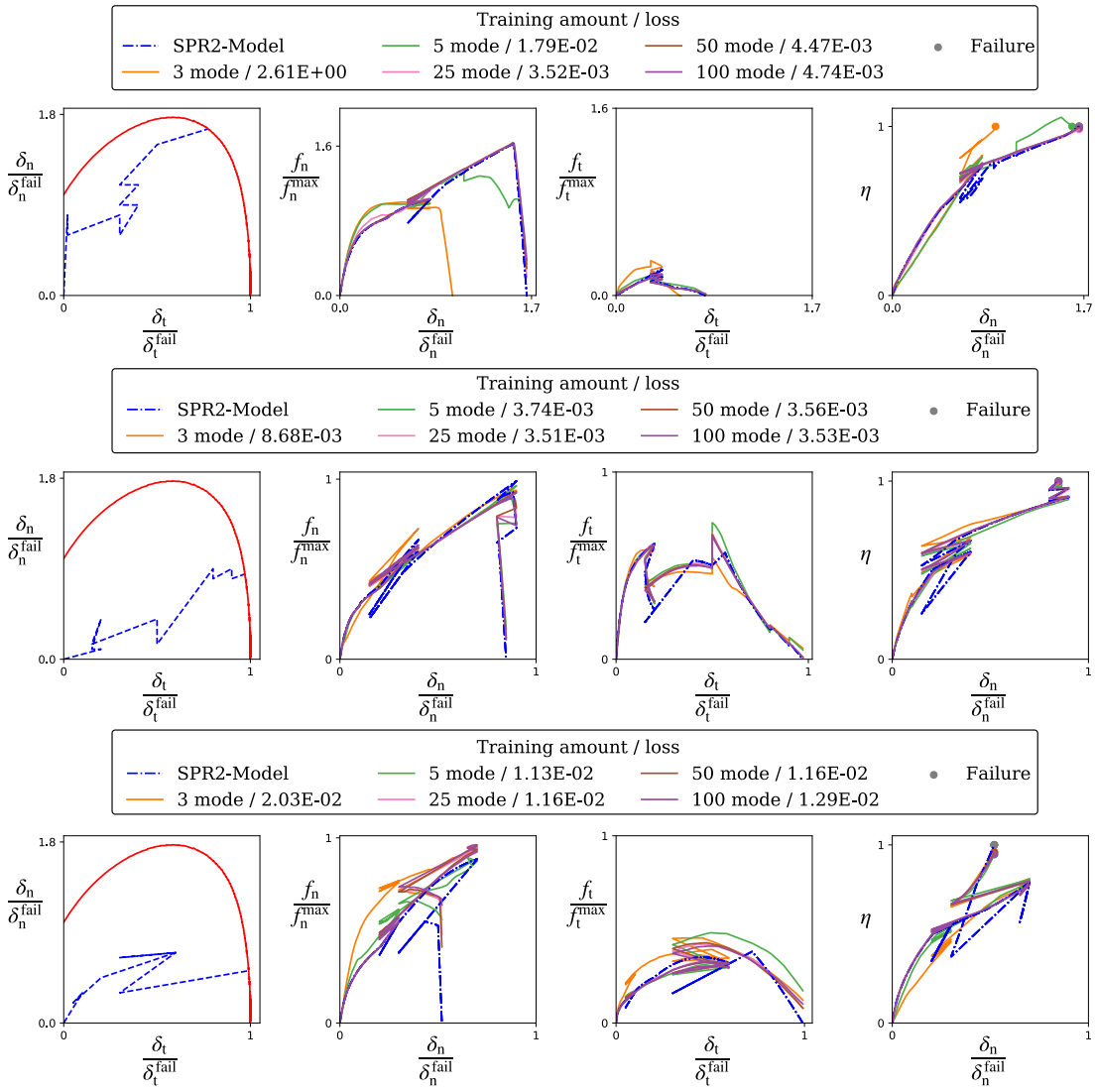

Fig. 19. NN trained on proportional loading with varying mode amount; three exemplary load cases with mode change and unloading/reloading, parameters from FDS01.

5.1. Virtual evaluation FDS01

Fig. 18 shows the failure loci of FDS01 for proportional loading. The discretisation between normal and tangential loading ranged from 3 to 100 modes. The NN trained with at least 25 modes gave a good fit compared to the fully trained NN from Section 3.3. A NN trained with 10 modes gave a good fit for lower maximum effective displacement values but a worse fit close to failure. The effect for networks trained with non-proportional paths and unloading/reloading are not shown in the failure loci diagrams but were evaluated on arbitrarily generated stretch paths.

Fig. 19 shows the predictions made by the networks, which were only trained on the proportional loading paths. The stretch paths used for validation included sudden mode changes and unloading/reloading. While training on only three and five modes gave a deviation in the force level, the predictions with a 25, 50 and 100 mode training gave a good representation of the force level and also copied the evolution of maximum effective displacement. The unloading paths could not be reproduced, but the joint stiffness was maintained and kept in a similar range. The results from the networks trained on unloading are shown in Fig. 20. They show better prediction capabilities for unloading compared to networks trained only on proportional loading. Fig. 21 shows an equal performance from a NN trained on non-proportional loading as a NN trained on proportional loading. There were more training paths with non-proportional loading than with proportional due to the combination with the mode changes. A NN trained on non-proportional paths did not seem to outperform a NN trained on only proportional loading when challenged with the arbitrary load cases.

5.2. Component evaluation FDS01

Two network designs, one trained only on proportional loading with 25 modes and one network trained on unloading, were compared for the component simulation. The training with unloading consisted of five modes and five unloading positions giving as well 25 paths, so that both NNs saw an equal number of training paths. The global force–displacement response is compared to the simulation with the fully trained NN and the simulation applying the model by Hanssen applied to cohesive elements (see Fig. 22). Due to the folding motion of the component, governing the force-response, no large deviations between the models can be observed. The local stress response from the cohesive

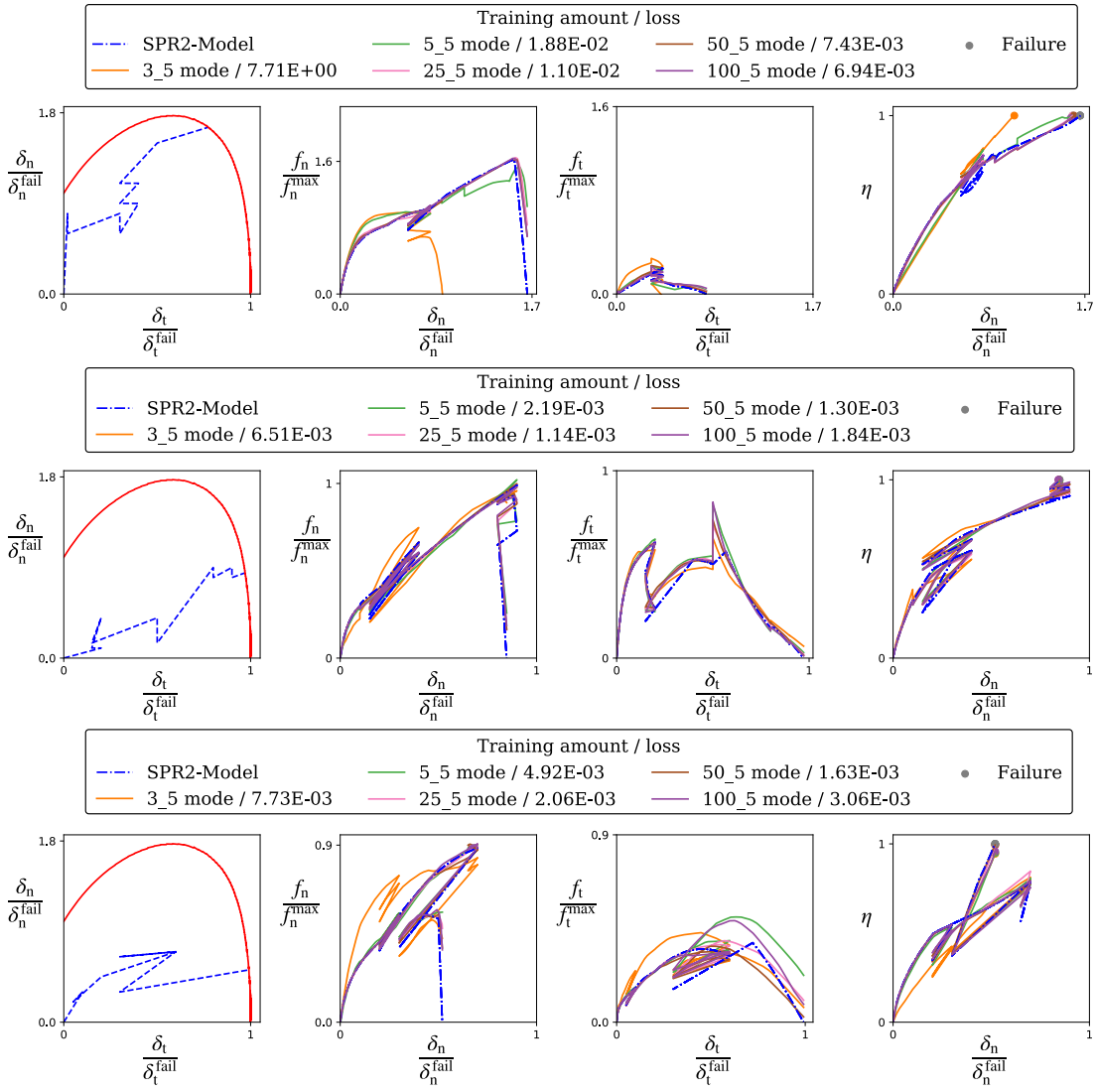

Fig. 20. NN trained on varying amount of load/unloading paths (fixed number of five unloading points); the amount of training paths is the number of modes multiplied by 5; there are three arbitrary load cases with mode change and unloading/reloading, parameters from FDS01.

elements in the component simulations can be seen in Figs. 23 and 24 where they are compared to the fully trained NN (see Section 4.3.1) and the constraint model. While the force response was captured quite well by the two partially trained NN, both showed deviation at failure especially in cohesive elements V and VI with an increased normal cohesive force. Both partially trained networks were not able to capture the point of failure in cohesive element V. Even though the joints in the crash box simulation experienced unloading and complex mode changes, the partially trained networks performed quite well compared to the Hanssen model. Although one NN was not trained on unloading paths, it gave reasonable results in the unloading phase and maintained the force level.

5.3. Component evaluation FDS04

The comparison between the fully and partially trained NNs for modelling of FDS04 is seen in Fig. 25. The effect of partially trained NNs was not investigated for FDS03 as the joint was not challenged much during the component test. The 5/5 load/unload NN showed an increased peak force and failure initiation at a larger displacement while the proportional loading NN resembled the full trained model with slightly later failure at the last two force drops. The global response can be explained by evaluating the local behaviour (see Fig. 26) where the increased force level in the 5/5 load/unload model is visible. While the proportional loading model depicts the Hanssen model and fully trained NN model quite well, the NN trained on load/unloading paths shows the late failure initiation. All NN models reached the point of failure in cohesive elements I, II and III while the model by Hanssen only reached failure in elements I and II.

6. Conclusions

A constitutive model for describing the force–deformation behaviour for a constraint model was replaced by a feedforward NN and applied to five different joint configurations. The constraint models were calibrated with cross tests and the parameters were used to create

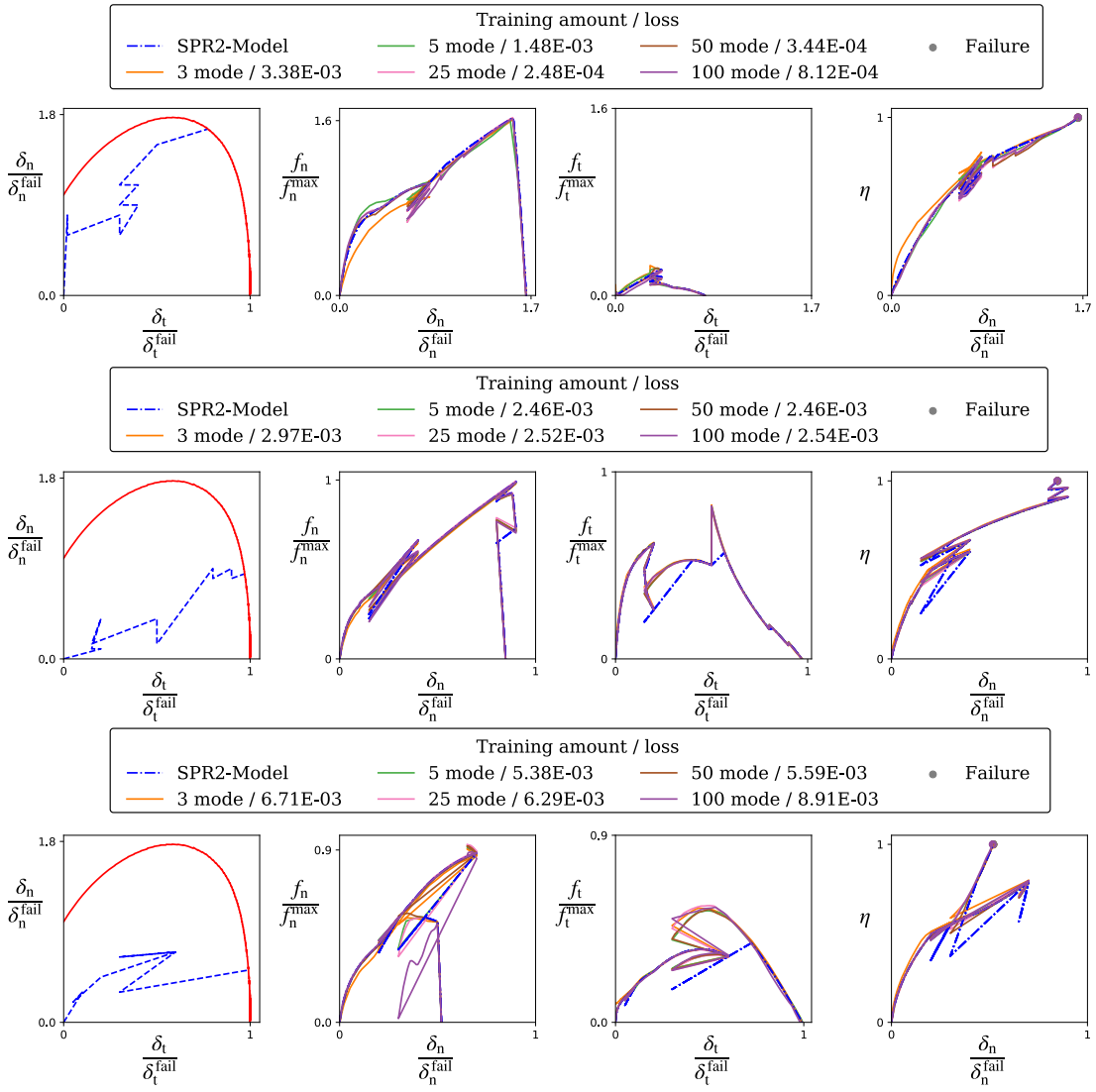

Fig. 21. NN trained on varying amount of non-proportional paths and 10 points where the mode changed; the amount of training paths is the number of modes multiplied by 10; there are three arbitrary load cases with mode change and unloading/reloading, parameters from FDS01).

virtual load paths for training the neural networks. Both the NN and the constraint model equations were implemented as cohesive material. The NN model and the constraint model could be used in form of cohesive elements. The NN model was first verified with single connector cross tests and validated with component tests. The results were compared on a global force–displacement level and by the local stress–stretch response. The following conclusions were drawn:

- One common feedforward NN architecture was able to represent the behaviour of five joints, namely one self-piercing rivet and four different flow-drill screws.
- The amount of training data and necessary load paths for the NN were evaluated. It was shown that even with a reduced amount of training data, a reliable neural network fit was achieved.
- The NN was able to give reliable predictions of the failure loci even after relatively scarce representation of loading directions.
- The NN could make reasonable predictions for unloading situations even when it was not trained on them.
- The NN model was compared to the constraint model in single joint tests and component tests where the NN model showed reasonable performance.

Numerical techniques like NN-modelling could be used in the future to increase the accuracy of joint models in FE analyses. Large amounts of data would be generated by detailed mesoscopic modelling of joint behaviour subjected to different load combinations. The dataset could then be used for training of a NN, to represent the behaviour of the mechanical joint in a large-scale analysis.

CRediT authorship contribution statement

Victor André: Conceptualisation, Formal analysis, Data curation, Visualization, Writing – original draft. **Miguel Costas:** Supervision, Writing – review & editing. **Magnus Langseth:** Funding acquisition, Supervision, Writing – review & editing. **David Morin:** Conceptualisation, Supervision, Project administration, Writing – review & editing.

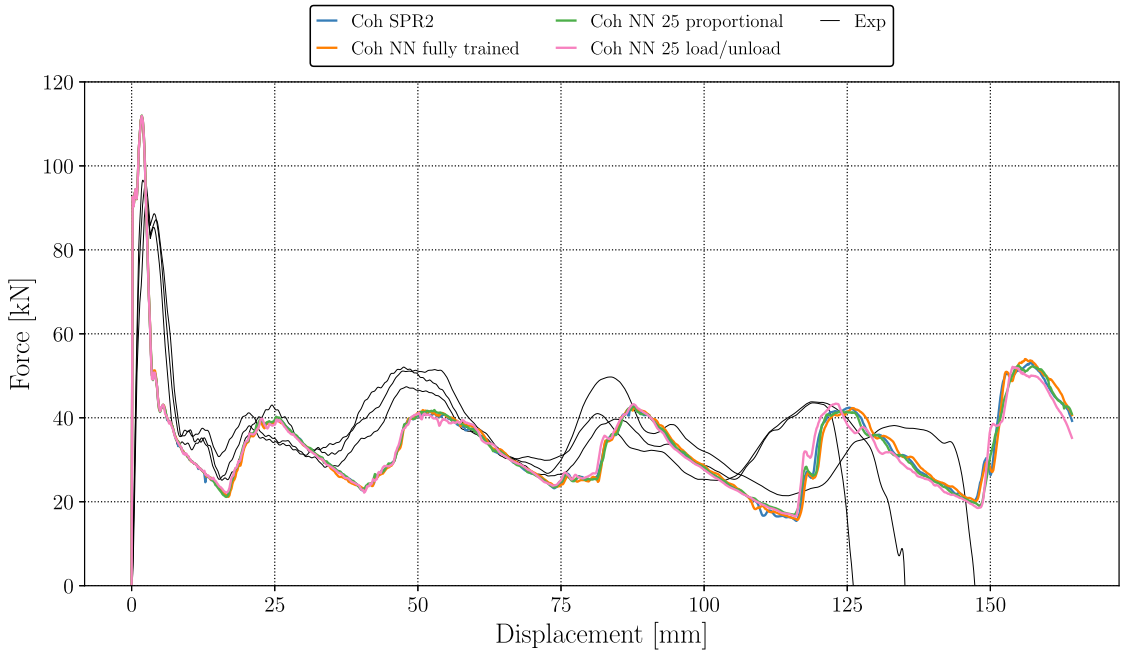

Fig. 22. FDS01 axial crushing, global force–displacement simulation (joint FDS01) compared to experiments, full and partially trained NN.

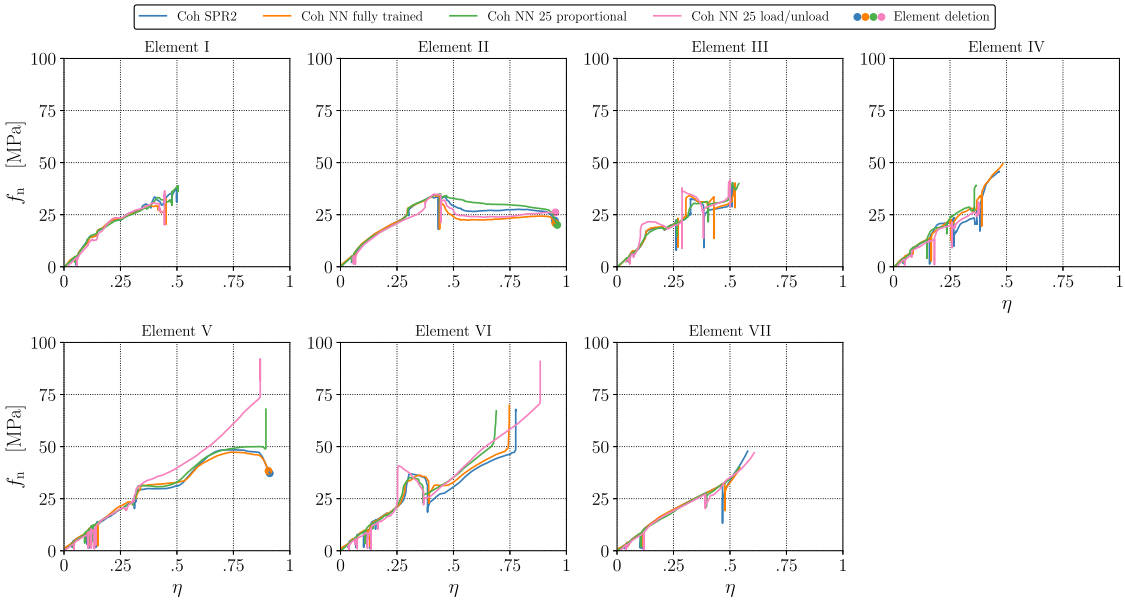

Fig. 23. Normal force f_n versus maximum effective displacement η; force normalised by cohesive element area; for FDS01.

Declaration of competing interest

The authors declared no potential conflicts of interest with respect to the research, authorship, and/or publication of this article.

Data availability

Data will be made available on request.

Acknowledgements

The authors would like to acknowledge the financial support from the Centre for Advanced Structural Analysis, SFI-CASA (Project No. 237885), funded by the Research Council of Norway and NTNU, Norway.

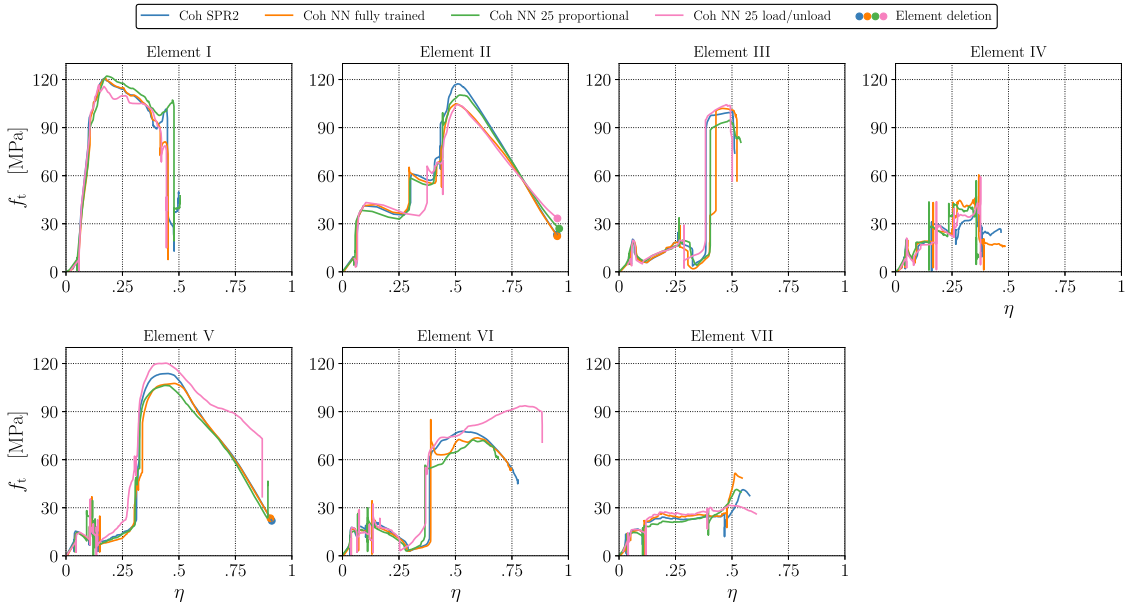

Fig. 24. Tangential force f_t versus maximum effective displacement η; force normalised by cohesive element area; for FDS01.

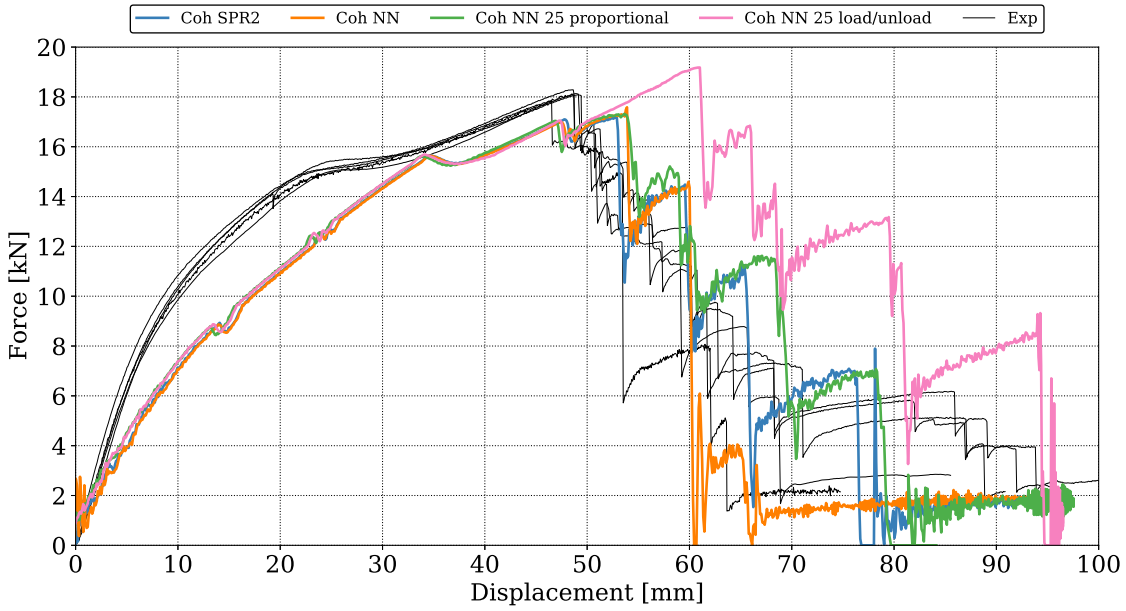

Fig. 25. Global force–displacement response, FDS03 full trained, FDS04 partially trained.

Table A.3
Constraint model parameters for each joint type; deformation to failure given in mm; force given in MPa.

JointID	Top sheet	Bottom sheet	δ_n^{fail}	δ_t^{fail}	f_n^{max}	f_t^{max}	ξ_n	ξ_t	α_1	α_2	α_3
SPR01	AA6016 T4 2.0 mm	AA6016 T4 2.0 mm	7.0	6.0	42.0	73.0	0.9	0.6	0.124	0.488	1.750
FDS01	AA6016 T4 2.0 mm	AA6016 T4 2.0 mm	3.2	5.0	107.5	190.0	0.95	0.5	0.108	0.436	1.878
FDS02	AA6016 T4 2.0 mm	AA6063 T6 2.0 mm T6	3.5	16.0	108.0	230.0	0.72	0.45	0.05	1.169	2.0
FDS03	AA6060 T6 2.5 mm	AA6060 T6 2.5 mm	4.6	23.0	65.0	117.0	0.98	0.6	1.812	1.24	0.956
FDS04	AA6060 T6 2.5 mm	AA6005 T6 2.5 mm T6	4.6	21.0	88.8	135.0	0.95	0.6	1.17	1.23	0.788

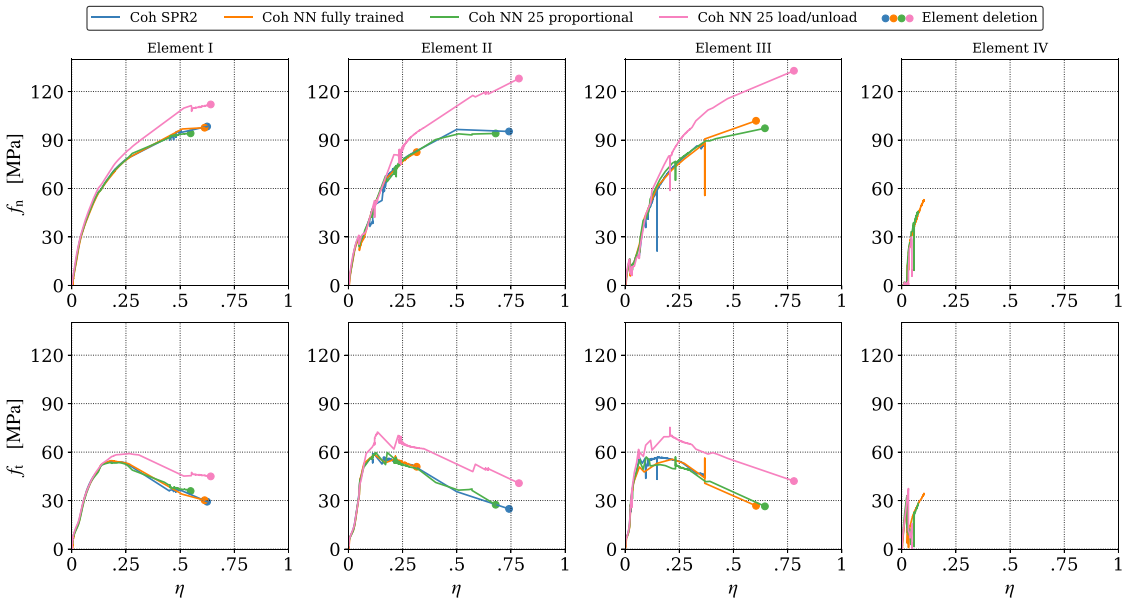

Fig. 26. Normal force f_n (top) and tangential force f_t (bottom) versus effective maximum displacement η; forces normalised by cohesive element area; see element labelling Fig. 15).

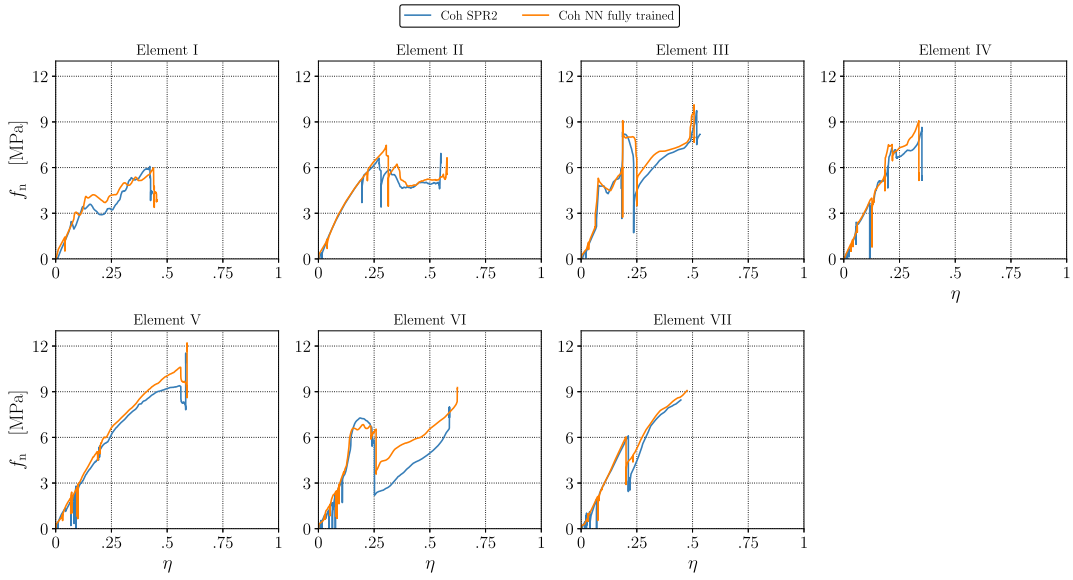

Fig. B.27. SPR01: Normal force f_n versus maximum effective displacement η; force normalised by cohesive element area.

Table A.4
Material model parameters are given with a Young's modulus of 70 GPa and a Poisson's ratio of 0.3; the Voce hardening parameters are given in MPa.

Material	σ_0	Q_{R1}	θ_{R1}	Q_{R2}	θ_{R2}	Q_{R3}	θ_{R3}
AA6016 T4 2.0 mm	117.6	29.2	25000.0	149.5	2011.0	100.0	230.0
AA6063 T6 2.0 mm	204.6	8.0	12300.0	55.0	1472.0	0.0	0.0
AA6060 T6 2.5 mm	183.2	2.5	5746.3	52.1	985.7	0.0	0.0
AA6005 T6 2.5 mm	275.7	8.6	7095.1	48.5	702.3	12.2	166.2

Appendix A. Material and constraint modelling

This is the isotropic plasticity model used for modelling the plate material. The Hershey-Hosford yield criterion with an exponent of 8 and Voce-hardening [25] were applied. The yield function can be written as

$$f = \sigma_{\text{eq}} - (\sigma_0 + R) \leq 0, \tag{A.1}$$

where σ_{eq} is the equivalent stress, σ_0 the initial yield stress and R is the isotropic hardening variable. The equivalent stress σ_{eq} is given as

$$\sigma_{\text{eq}} = \sqrt[n]{\frac{1}{2}|\sigma_2 - \sigma_3|^n + \frac{1}{2}|\sigma_3 - \sigma_1|^n + \frac{1}{2}|\sigma_1 - \sigma_2|^n} \tag{A.2}$$

which is a generalised form of the von Mises equivalent stress with the material dependent exponent $n = 8$, and the principal stresses σ_1, σ_2 and σ_3. The hardening variable R is given by the Voce hardening law,

$$R = \sum_{i=1}^{N} Q_{\text{R}i} \left(1 - \exp\left(-\frac{\theta_{\text{R}i}}{Q_{\text{R}i}} p\right)\right), \tag{A.3}$$

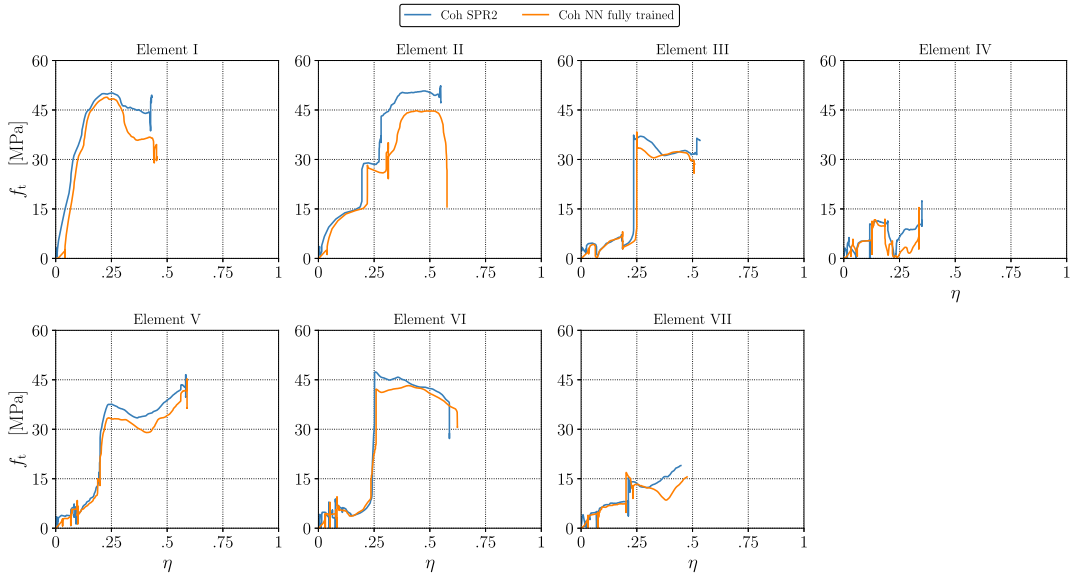

Fig. B.28. SPR01: Tangential force f_t versus maximum effective displacement η; force normalised by cohesive element area.

where N is the number of terms used, and Q_{Ri} and θ_{Ri} are the final stress where hardening saturates and the initial hardening modulus. The term is denoted with i.

Appendix B. Crash box simulation with SPR01

Figs. B.27 and B.28 show the local response from the cohesive elements in the crash box simulation with joint SPR01. The response from the NN model is in good accordance with the cohesive elements applying the Hanssen-model. Loading and reloading could be replicated but no element deletion occurred in neither of the two simulations.

References

[1] Sun X, Khaleel MA. Dynamic strength evaluations for self-piercing rivets and resistance spot welds joining similar and dissimilar metals. Int J Impact Eng 2007;34(10):1668–82. http://dx.doi.org/10.1016/J.IJIMPENG.2006.09.092.

[2] Kõrgesaar M, Remes H, Romanoff J. Size dependent response of large shell elements under in-plane tensile loading. Int J Solids Struct 2014;51(21–22):3752–61. http://dx.doi.org/10.1016/J.IJSOLSTR.2014.07.012.

[3] Combescure A, Delcroix F, Caplain L, Espanol S, Eliot P. A finite element to simulate the failure of weld points on impact. Int J Impact Eng 2003;28(7):783–802. http://dx.doi.org/10.1016/S0734-743X(02)00158-6.

[4] Sønstabø JK, Morin D, Langseth M. Macroscopic modelling of flow-drill screw connections in thin-walled aluminium structures. Thin-Walled Struct 2016;105:185–206. http://dx.doi.org/10.1016/j.tws.2016.04.013.

[5] Reil M, Morin D, Langseth M, Knoll O. A novel tests set-up for validation of connector models subjected to static and impact loadings. Int J Impact Eng 2021;158(June):103978. http://dx.doi.org/10.1016/j.ijimpeng.2021.103978.

[6] Porcaro R, Hanssen AG, Aalberg A, Langseth M. Joining of aluminium using self-piercing riveting: Testing, modelling and analysis. Int J Crashworthiness 2004;9(2):141–54. http://dx.doi.org/10.1533/ijcr.2004.0279.

[7] Hanssen AG, Olovsson L, Porcaro R, Langseth M. A large-scale finite element point-connector model for self-piercing rivet connections. Eur J Mech A 2010;29(4):484–95. http://dx.doi.org/10.1016/j.euromechsol.2010.02.010.

[8] Marzi S, Hesebeck O, Brede M, Kleiner F. A rate-dependent, elasto-plastic cohesive zone mixed-mode model for crash analysis of adhesively bonded joints. In: 7th European LS-Dyna conference. 2009.

[9] Bier M, Liebold C, Haufe A, Klamser H. Evaluation of a rate-dependent, elasto-plastic cohesive zone mixed-mode constitutive model for spot weld modeling. In: 9th LS-DYNA forum. 2010.

[10] Bonatti C, Mohr D. On the importance of self-consistency in recurrent neural network models representing elasto-plastic solids. J Mech Phys Solids 2021;158(November):104697. http://dx.doi.org/10.1016/j.jmps.2021.104697.

[11] Bock FE, Aydin RC, Cyron CJ, Huber N, Kalidindi SR, Klusemann B. A review of the application of machine learning and data mining approaches in continuum materials mechanics. Front Mater 2019;6(May). http://dx.doi.org/10.3389/fmats.2019.00110.

[12] Burton H, Mieler M. Machine learning applications: Hope, hype, or hindrance for structural engineering. Struct Mag 2021;(June):16–20.

[13] Livermore Software Technology Corporation. LS-DYNA version R9.3.1 documentation. Livermore, California, US; 2016.

[14] Sønstabø JK, Holmstrøm PH, Morin D, Langseth M. Macroscopic strength and failure properties of flow-drill screw connections. J Mater Process Technol 2015;222:1–12. http://dx.doi.org/10.1016/j.jmatprotec.2015.02.031.

[15] Sønstabø JK, Morin D, Langseth M. Static and dynamic testing and modelling of aluminium joints with flow-drill screw connections. Int J Impact Eng 2018;115(January):58–75. http://dx.doi.org/10.1016/j.ijimpeng.2018.01.008.

[16] Sønstabø JK, Morin D, Langseth M. Testing and modelling of flow-drill screw connections under quasi-static loadings. J Mater Process Technol 2018;255:724–38. http://dx.doi.org/10.1016/j.jmatprotec.2018.01.007.

[17] Chollet F. Keras. 2015, GitHub, URL https://github.com/fchollet/keras.

[18] Porcaro R, Langseth M, Hanssen AG, Zhao H, Weyer S, Hooputra H. Crashworthiness of self-piercing riveted connections. Int J Impact Eng 2008;35(11):1251–66. http://dx.doi.org/10.1016/j.ijimpeng.2007.07.008.

[19] Gorji MB, Mohr D. Towards neural network models for describing the large deformation behavior of sheet metal. IOP Conf Ser Mater Sci Eng 2019;651(1). http://dx.doi.org/10.1088/1757-899X/651/1/012102.

[20] Nesterov Y. A method for solving the convex programming problem with convergence rate O(1/k2). Dokl Akad Nauk SSSR 1983;269:543–7.

[21] Glorot X, Bordes A, Bengio Y. Deep sparse rectifier neural networks. In: Gordon Geoffrey, Dunson David, Dudík Miroslav, editors. Proceedings of the fourteenth international conference on artificial intelligence and statistics, vol. 15. Fort Lauderdale, FL, USA: PMLR; 2011, p. 315–23. http://dx.doi.org/10.1002/ecs2.1832.

[22] Shanker MS, Hu MY, Hung MS. Effect of data standardization on neural network training. Omega 1996;24(4):385–97. http://dx.doi.org/10.1016/0305-0483(96)00010-2.

[23] Fahlmann SE, Lebiere C. The cascade-correlation learning architecture. Adv Neural Inf Process Syst 1990;524–32.

[24] Nakama T. Comparisons of single- and multiple-hidden-layer neural networks. In: Liu D, Zhang H, Polycarpou M, Alippi C, He H, editors. Advances in neural networks. Berlin, Heidelberg: Springer; 2011, p. 270–9. http://dx.doi.org/10.1007/978-3-642-21105-8_32.

[25] Hershey A. The plasticity of an isotropic aggregate of anisotropic face-centered cubic crystals. J Appl Mech Trans ASME 1954;241–9.